Section III
Theories and Dynamics

6

Simple ENSO Models

Fei-Fei Jin[1], Han-Ching Chen[1], Sen Zhao[1], Michiya Hayashi[1,#], Christina Karamperidou[1], Malte F. Stuecker[2,3,4,5,*], Ruihuang Xie[6], and Licheng Geng[1]

ABSTRACT

The fundamental dynamical mechanisms of the El Niño-Southern Oscillation (ENSO) phenomenon have been extensively studied since Bjerknes envisioned ocean-atmosphere interaction in the equatorial Pacific as its main cause. This chapter provides a review of the recent progress in ENSO theory based on two classes of relatively simple models: (i) the Cane-Zebiak (CZ) type models of intermediate complexity and (ii) conceptual low-order models reducible from the CZ-type models. The leading mode of ENSO variability, in reanalysis data, the CZ-type models, and comprehensive climate models, can be reduced into the simplest possible coupled oscillator known as the recharge oscillator (RO). Incorporating seasonality, nonlinearity, and multiscale processes into the RO framework, allows for basic understanding of how key physical processes determine ENSO's properties, such as its amplitude, periodicity, phase-locking, asymmetry, and nonlinear rectification onto the mean state. As these key physical processes can be easily quantified in both model and reanalysis data, the RO framework can be used to assess the simulations and projections of ENSO in climate models.

6.1. INTRODUCTION

The early stages of understanding and modeling of the ENSO phenomenon were marked by the seminal papers of Bjerknes (1969), Wyrtki (1985), and Cane and Zebiak (1985). These three visionary studies advanced a clear hypothesis that casts ENSO as a phenomenon originating from an oscillatory coupled ocean-atmosphere instability. First, Bjerknes (1969) hypothesized that ENSO SST anomalies (SSTAs) can grow via reorganizing of the equatorial Pacific trade winds and altering of the ocean mixed-layer heat budget through horizontal currents and upwelling. Then, Wyrtki (1985) noted that in order for a phase transition to occur and for ENSO to be cyclic, a redistribution of heat content driven by the trade winds is required, namely, a slow recharge of warm water in the western Pacific before the onset of El Niño and a discharge after its peak. Meanwhile, Cane and Zebiak (1985) built the first dynamical ENSO model to successfully test the above hypotheses. While these hypotheses for ENSO growth and its phase transitions were based on very limited data, and the Cane-Zebiak model is of modest complexity, they set the stage for the advancement of ENSO theory, modeling, and prediction for years to come.

Decades' worth of research studies since then viewed ENSO as a coupled ocean-atmosphere mode (i.e., a spatially and temporally coherent pattern of covariability in

[1]*Department of Atmospheric Sciences, SOEST, University of Hawai'i at Mānoa, Honolulu, HI, USA*

[2]*Department of Oceanography, SOEST, University of Hawai'i at Mānoa, Honolulu, HI, USA*

[3]*International Pacific Research Center, SOEST, University of Hawai'i at Mānoa, Honolulu, HI, USA*

[4]*Center for Climate Physics, Institute for Basic Science, Busan, Republic of Korea*

[5]*Pusan National University, Busan, Republic of Korea*

[6]*Key Laboratory of Ocean Circulation and Waves, Institute of Oceanology, Chinese Academy of Sciences, Qingdao, China*

**now at the University of Hawai'i at Mānoa, HI, USA*

[#] now at Center for Global Environmental Research, National Institute for Environmental Studies, Tsukuba, Ibaraki, Japan

El Niño Southern Oscillation in a Changing Climate, Geophysical Monograph 253, First Edition.
Edited by Michael J. McPhaden, Agus Santoso, and Wenju Cai.

oceanic and atmospheric variables that arises from their dynamical coupling) that can be described on the basis of linear instability theory using relatively simple coupled models that eventually boil down to the delayed and recharge oscillator paradigms (e.g., Cane & Zebiak, 1985; Gill, 1985; Hirst, 1986; Suarez & Schopf, 1988; Battisti & Hirst, 1989; Philander, 1990; Neelin, 1990; Jin & Neelin, 1993a, 1993b; Neelin & Jin, 1993; Neelin et al., 1994; Jin, 1997a, 1997b; Neelin et al., 1998; Wang et al., 1999). ENSO behaviors observed in nature or simulated in various coupled models were viewed qualitatively as the result of a sensitive dependence of the leading coupled modes to variations in the climate background state or in physical parameters related to the ocean-atmosphere coupling (e.g., Philander et al., 1984; Jin & Neelin, 1993a; An & Jin, 2000; Fedorov & Philander, 2000, 2001; Bejarano, 2006; Bejarano & Jin, 2008; Xie & Jin, 2018; Timmermann et al., 2018). The oscillatory nature of ENSO has been debated (Kessler, 2002; Philander & Fedorov, 2003; chapter 7 in this book), as it is being obscured by noise, nonlinearity, asymmetry, and abundant multiscale interactions. However, the largely linear view of ENSO described above has set the foundation for the understanding of fundamental ENSO dynamics. We will thus briefly review the progress that has been made on ENSO linear instability theory in section 6.2.

Adopting the principles of linear instability theory, a class of highly simplified conceptual models was developed since the 1980s, including the delayed oscillator (Suarez & Schopf, 1988; Battisti & Hirst, 1989), wave oscillator (Cane et al., 1990; Jin, 1997b), recharge oscillator (Jin, 1996, 1997a, 1997b), and advective-reflective oscillator (Picaut et al., 1997). Despite their simplifications and their limitations in explaining the observed ENSO spatial pattern diversity and temporal complexity, most of these conceptual models are based on solid theoretical foundations and may be consolidated into a generalized recharge oscillator (RO) framework (Jin & An, 1999). This RO framework can be used to formulate a set of simple, approximate, but systematic measures for ENSO instability, namely, the Bjerknes and Wyrtki indices for ENSO linear growth rate and periodicity, respectively (Jin et al., 2006; Lu et al., 2018). This quantitative assessment of the ENSO instability indices using observational data and outputs from comprehensive coupled general circulation models (CGCMs) make the RO conceptual model framework a useful tool, particularly for connecting ENSO theory to observed and modeled ENSO behaviors under various background climate conditions. In section 6.3, we will discuss these simple conceptual models, their consolidation and generalization, and the formulation of the ENSO instability index, as well as its applications and limitations.

The role of seasonal modulation and stochastic and external forcing on ENSO dynamics and variability will be discussed in section 6.4, using linear and nonlinear versions of the conceptual models and the ENSO instability index. This chapter will end with a brief discussion of its connections to previous and following chapters and an outlook on future research and the role of conceptual models in a hierarchical approach to improve our understanding of ENSO dynamics in past, present, and future climates.

6.2. COUPLED LINEAR INSTABILITY

The observed variability of the coupled climate system and its underlying physical processes can be investigated via a study of the stability of a simplified linearized representation of the coupled climate system in the mathematical framework of dynamical systems. Similar to the role that baroclinic instability plays in the development of synoptic weather systems, coupled ocean-atmosphere instability is important for generating interannual variability in the tropical climate system. The frontal theory for cyclones by Bjerknes and Solberg (1922) and the coupled ocean-atmosphere positive feedback hypothesis for ENSO by Bjerknes (1969) foresaw the role of these two fundamental instabilities for Earth's dominant weather and climate systems. Advances in the understanding of tropical atmospheric waves and circulation (e.g., Matsuno, 1966; Webster, 1973; Gill, 1980; Zebiak, 1982; Lindzen & Nigam, 1987) and in parallel of tropical ocean dynamics (Moore, 1968; Cane & Sarachik, 1977, 1979, 1981; Cane, 1984) led to the ingenious formulation of the Cane-Zebiak (CZ) model, which was the first dynamical model that realistically simulated and predicted ENSO (Cane & Zebiak, 1985; Cane et al., 1986; Zebiak & Cane, 1987). Since then, CZ-type frameworks have become well-utilized tools in the advancement of ocean-atmosphere instability theory for ENSO (Gill, 1985; Hirst, 1986; Neelin, 1990; Jin et al., 1994; Jin, 1997a, 1997b; An & Jin, 2000; Fedorov & Philander, 2000, 2001; Bejarano & Jin, 2008; Xie & Jin, 2018; Timmermann et al., 2018).

6.2.1. Brief Description of the Cane-Zebiak Model

The CZ model is an anomaly model with a prescribed annually varying climate mean state (Figure 6.1a) and consists of simple atmospheric and oceanic components that can be derived from first principles with reasonable simplifications. As illustrated schematically in Figure 6.1b, it comprises a simple quasi-linear Gill-Matsuno atmospheric component (Gill, 1980; Zebiak, 1982; Zebiak & Cane, 1987; also see the appendix to this chapter) that simulates the tropical wind response to ENSO-associated SST anomalies. Its oceanic dynamical component is a 1.5-layer linear reduced gravity model that describes the

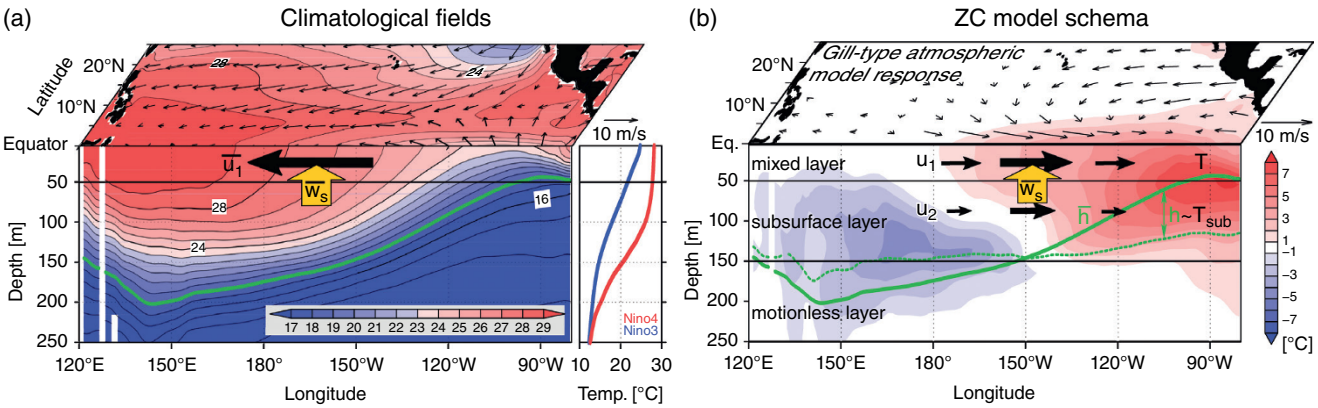

Figure 6.1 Schematic diagrams for the Cane-Zebiak (CZ) model. (a) Climatological states prescribed for the model. Horizontal plane: mean SST (shadings) and surface winds (vector). Vertical plane: mean vertical ocean temperature profile along equator (shadings, left panel), and in the Niño-4 (red line, right panel) and Niño-3 (blue line, right panel) regions. Embedded black arrow indicates mean zonal current in the mixed layer, and orange arrow denotes mean upwelling. The 18°C isotherm is highlighted as thermocline. (b) Schematic for CZ model dynamics. Horizontal plane: Simulated Gill-Matsuno wind response (vectors) to observed SSTAs (shadings) averaged between October 1997 and February 1998 (example El Niño event). Vertical plane: observed ocean temperature anomalies (shadings) in the same period and simulated thermocline depth (green dashed line). The thick black arrows schematically present the simulated anomalous ocean current in the mixed layer 1 and subsurface layer 2. The change in the thermocline depth (h) is used to derive the ocean temperature anomalies in the subsurface (T_{sub}), which further influence SSTA (T) through Eq. A4a.

upper-layer current and thermocline depth anomalies in response to wind anomalies. Within this upper layer ocean there is an embedded mixed layer with a fixed depth and an underlying subsurface layer with a prescribed mean depth. This approximation in representing the vertical structure of ocean dynamics allows the CZ oceanic model to simulate anomalous horizonal and vertical velocities in the mixed layer and at the mixed-layer base, respectively. By introducing an assumption that subsurface ocean temperature is adiabatically redistributed following the thermocline depth variations, the CZ model captures to a large extent mixed-layer SSTA dynamics governed by the heat budget equation (Zebiak & Cane, 1987; also see the appendix for details).

The atmosphere and ocean are coupled in the CZ model by three main closure approximations: (i) an approximation for wind-driven ocean current anomalies in the mixed layer that combines a vertically sheared current from an Ekman-flow model with an upper-layer current from the reduced-gravity wave dynamics model, (ii) a nonlinear relation between the subsurface ocean temperature and the thermocline depth, partly motivated by the dependence of the vertical profiles on the thermocline depth (Figure 6.1a), and (iii) a parameterized atmospheric heating anomaly in response to SSTA and atmospheric moisture convergence anomalies in the Gill model framework (see Zebiak & Cane, 1987, and the appendix for details). Importantly, the CZ model focuses on the dynamical coupling processes: SSTA yields wind stress anomalies, which produce horizontal current and upwelling anomalies, as well as subsurface temperature anomalies that are related to dynamic redistribution of ocean heat and thereby feed back onto SSTA. The complex thermodynamic surface heat flux feedbacks are greatly simplified by assuming a constant Newtonian SSTA damping. By focusing on the dynamical coupling in the tropical Pacific domain (29°S–29°N, 124°E–80°W), this model provides a simple coupled framework that fully embodies the key hypotheses for the coupled dynamical feedbacks contributing to ENSO growth as envisioned by Bjerknes (1969), and the ENSO turnabout mechanism through upper ocean heat content redistribution envisioned by Wyrtki (1985), that allows for ENSO to oscillate between El Niño and La Niña phases.

6.2.2. Linear ENSO Stability Analysis in the CZ Model

The CZ model framework has been the foundation for the advancements of ENSO linear instability theory in the past 30 years. The concept of linear ENSO instability helps us to understand the fundamental ENSO dynamics by exploring the most unstable intrinsic mode in a dynamical system described by many simple-to-intermediate complexity models. Early work of ENSO instability theory (Gill, 1985; Hirst, 1986; Battisti & Hirst, 1989; Neelin, 1990; Jin & Neelin, 1993a, 1993b; Neelin & Jin, 1993 (together JN93 hereafter); Jin et al., 1994; Jin, 1997a, 1997b; An & Jin, 2000; Fedorov & Philander, 2000, 2001)

was largely based on simpler versions of the CZ model. For example, by considering the SSTA equation only within the equatorial strip instead of the entire tropical Pacific basin, JN93 developed a stripped-down version of CZ model with its full ocean wave dynamics component, as described in the appendix. This slightly simplified CZ-type model allows for thorough analytical and numerical eigen-analyses of the leading coupled mode in wide ranges of the parameter spaces and thus a basic understanding of how key coupled processes give rise to ENSO-like modes (JN93). By converting the parameter spaces to mean state spaces, An and Jin (2000) and Fedorov and Philander (2000, 2001) used the instability theory based on the JN93 stripped-down model to investigate the diverse ENSO behaviors simulated in climate models under past, present, and future mean climate conditions. There is one ENSO-like leading mode that stands out from the large continuum of eigen modes in the various simplified versions of the CZ model, such as the JN93 stripped-down version and a two-strip model which further reduced the ocean equatorial wave dynamics within the equatorial and off-equatorial strips (Jin, 1997b). This type of ENSO eigen mode analysis was carried out in linearized versions of the full CZ model (Bejarano, 2006; Bejarano & Jin, 2008; Xie & Jin, 2018) with respect to a broad range of both parameter space and basic-state space. In these studies, the leading ENSO mode is largely near critical (i.e., subcritical/supercritical when their growth rates are slightly negative/positive) within a realistic range of the parameter and basic state spaces. When subcritical, it can be easily excited by stochastic forcing, and when supercritical it can be self-sustained (linear growth will be constrained by nonlinear dynamic damping). Thus, the leading ENSO mode tends to dominate the internal variability in a manner similar to the observed ENSO behavior.

Here we give a brief account of the behaviors of the leading mode in the CZ model based on a recalculation of eigen solutions of the CZ model because the earlier eigen analyses by Bejarano (2006), Bejarano and Jin (2008), as well as Xie and Jin (2018) shared a coding error that corrupted their eigen solutions (it was recently uncovered by Mr. Licheng Geng while working on his PhD thesis on the subject). This error results in an artificial split of the single leading oscillatory ENSO-like mode into two coexisting leading modes that were referred in Xie and Jin (2018) as EP and CP ENSO modes, as their SST patterns happened to resemble EP and CP El Niño patterns. After the error was cleared, the CZ model in fact allows only a single leading ENSO-like mode in broad basic state space (Figure 6.2a, b) and parameter space (Figure 6.2c, f), as in the earlier strip-down version models of JN93, An and Jin (2000), and Fedorov and Philander (2000). Consistent with the earlier studies, the growth rate and frequency of this leading ENSO mode vary sensitively in the parameter and basic state spaces (Figure 6.2). Two solutions marked as A and B in Figure 6.2 and 6.2b under relatively stronger (i.e., a stronger mean wind stress and thus colder SST in the cold tongue) and weaker (i.e., a weaker mean wind stress and thus a warmer SST in the cold tongue) cold tongue conditions display a moderate zonal shift in the mature SSTA pattern location, albeit much less than seen in the observations for CP and EP events (Figure 6.3b, f). However, there is a remarkable large difference in the linear frequency. It shifts from quasi-biannual (QB) to quasi-quadrennial (QQ) periodicity ranges when the basic state is changed from a relatively stronger cold-tongue state (A) to a weaker cold-tongue state (B). This strong dependence of the ENSO mode on the strength of the cold tongue basic state is important for understanding ENSO complexity as it is partly responsible for the ENSO pattern diversity simulated in CZ models as noted in Bejarano and Jin (2008) and Xie and Jin (2018) in their nonlinear solutions. Further detailed discussion on this subject will be presented in forthcoming papers.

6.2.3. Dynamical Mechanisms Controlling Linear ENSO Mode

To gain insight into the dynamics of the leading ENSO mode in the linearized CZ model, one may examine the relative importance of the different terms that contribute to the SSTA tendency of the mode under different basic state conditions (Figure 6.3). Under a relatively weak cold-tongue basic state (point B in Figure 6.2a), the mode tends to have a QQ periodicity (Figure 6.2b). The dominant contribution for the SSTA growth rate is the thermocline (TH) feedback through upwelling of anomalous subsurface temperature, while the zonal advective (ZA) feedback via anomalous zonal current transport is of secondary importance (Figure 6.3d). In contrast, under a relative stronger cold-tongue basic state (point A in Figure 6.2a), the mode tends to have a QB periodicity (Figure 6.2b) and the role of the ZA feedback becomes similarly important as the TH feedback (Figure 6.3h). These different roles of ZA and TH were previously noted based on observational data analysis (Kug et al., 2009; Ren & Jin, 2013; Timmermann et al., 2018). In the CZ model, thermodynamics are implemented as a simple Newtonian SSTA damping, as indicated in Eq. (A4a). This is a major oversimplification in representing coupled thermodynamics in terms of how ENSO SSTA alters surface thermal fluxes through atmospheric moisture dynamics, radiative processes, and evaporative and sensible heat sources. Extending the CZ model framework to incorporate physically consistent thermodynamic coupling is needed to better understand how coupled thermodynamics may shape the patterns of this leading ENSO mode.

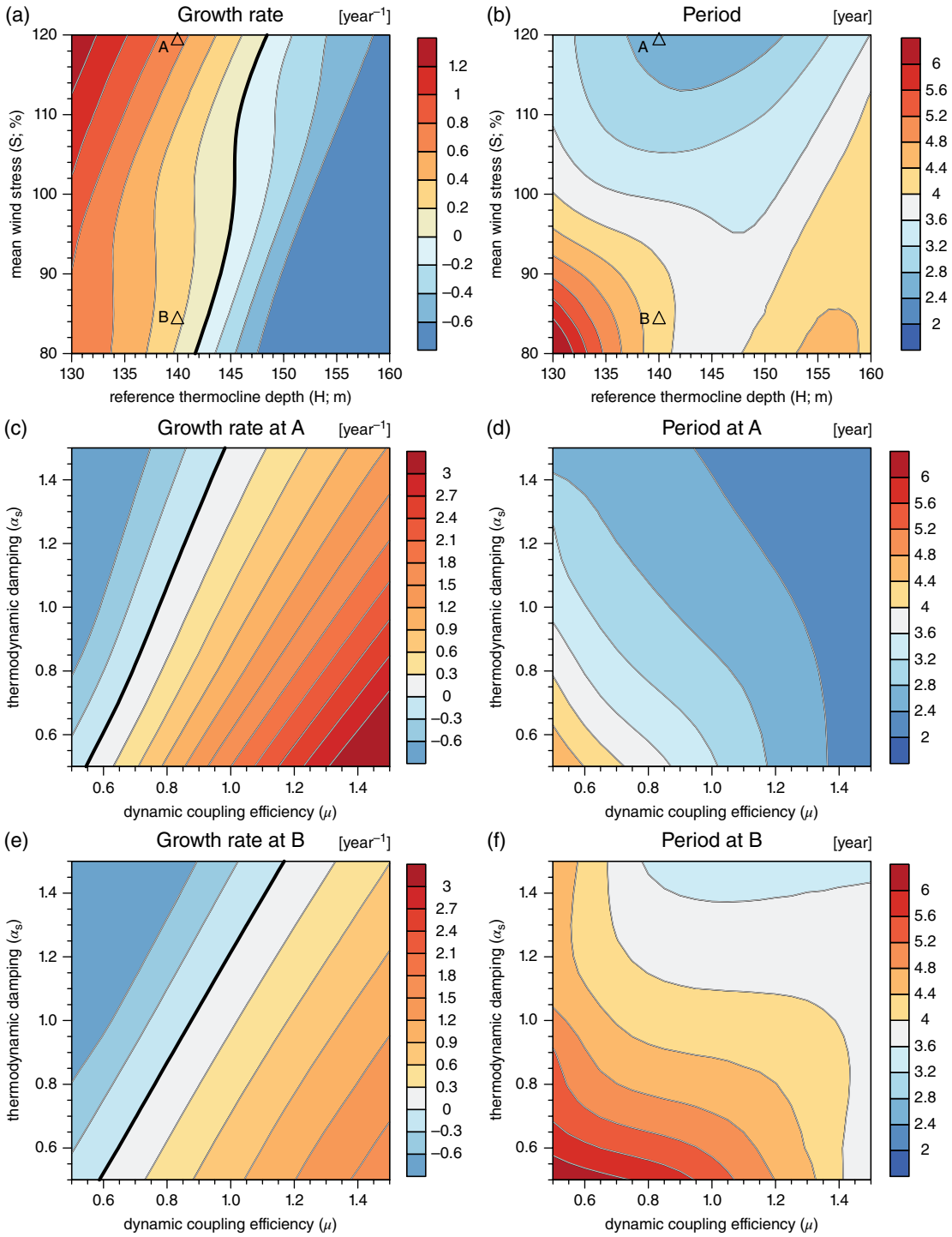

Figure 6.2 Instability of the leading ENSO mode as a function of the (a, b) basic states and (c–f) dynamic coupling efficiency (μ; *x*-axis) and thermodynamic damping relative to the default value in Table A (α_S; *y*-axis). Here, the basic state is characterized by the reference thermocline depth (H) in the model and the percentage change of the mean equatorial wind stress relative to the CZ standard configuration (S). Generally, the cold tongue SST is low when H is small and/or S is large, and vice versa (Xie & Jin, 2018). See Bejarano (2006) for the detailed description of how to produce these basic states. Figures c–f are the instability of the leading ENSO mode when perturbing parameters μ and α_S under the basic states at A and B. Values of μ = 1.0 and α_S = 1.0 correspond to the default model settings as in Zebiak and Cane (1987). Values of other parameters are listed in Table A. The units of growth rate and period are year^{-1} and year, respectively. These results were calculated by an eigen analysis of the linearized CZ model.

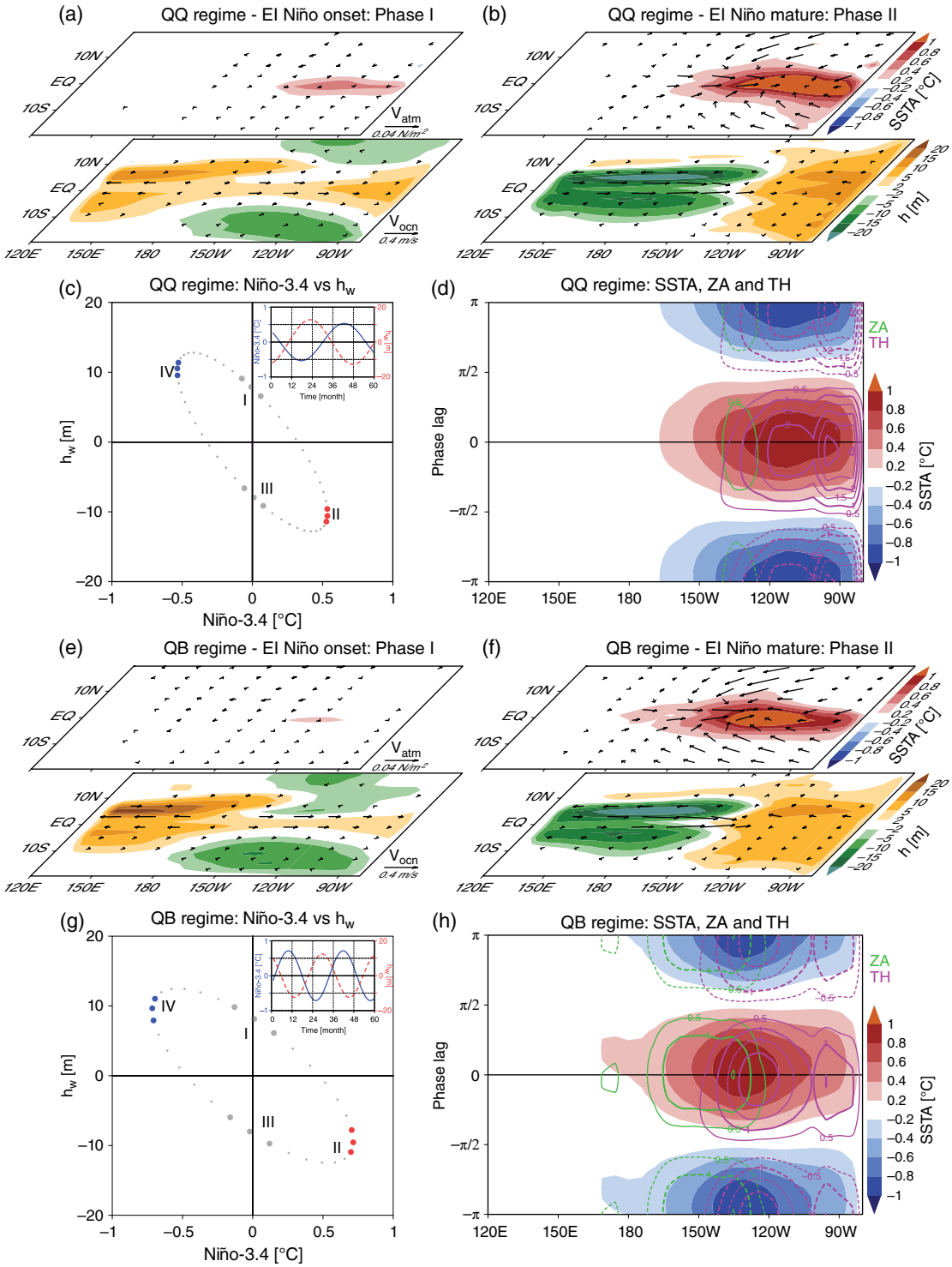

Figure 6.3 Schematic diagrams for the leading ENSO mode under weak (a–d) and strong (e–h) cold tongue basic states. In each phase, SST (shadings; °C) and wind stress (vectors; N m^{-2}) anomalies are shown in the upper panel, and thermocline depth (shadings; m) and mixed layer currents (vectors; ms^{-1}) in the bottom panel. Phases are determined from the (c, g) trajectories of Niño-3.4 index (°C; *x*-axis) and thermocline depth anomalies in the western Pacific (h_w; m; *y*-axis). See text for the definition of h_w. Onset phase I is a three-month average centered at the time when Niño-3.4 index ascends cross zero (gray dots), and mature phase II is centered at the time when Niño-3.4 index reaches the positive peak (red dots). Phases III and IV are opposite to phases I and II and indicate the transition and La Niña phases, respectively. Also shown are the time series of Niño-3.4 index and h_w in the upper-right corner. (d, h) Hovmöller diagrams of equatorial SSTA for 5°S–5°N (shadings) and the associated zonal advective (ZA; green contours) and thermocline (TH; purple contours) feedbacks for 2°S–2°N (10^{-1} °C $month^{-1}$) that contribute to the evolutions of SSTA. Phase $-\pi$ to phase π consists of a complete ENSO cycle.

The ENSO eigen mode displays strong sensitivity to changes in key parameters. Two such parameters are chosen as they are known to exhibit substantial ranges in CGCMs and because they have strong impacts on the growth rates and frequencies of the leading ENSO mode. The first is the dynamic coupling efficiency (μ) which is a control parameter multiplied onto the CZ model's atmospheric wind stress response to SSTA. The second is the thermodynamic damping (α_s) (see Eq. [A4a] and Table A of the appendix for details). The ENSO mode becomes unstable when the dynamic coupling efficiency increases and/or the thermodynamic damping decreases (Figure 6.2c, e). Interestingly, the growth rate contours are nearly diagonal under both relative weak and strong cold-tongue basic states, indicating a strong compensation effect on ENSO growth rate from dynamic coupling efficiency and thermodynamic damping, which is consistent with findings of strong error compensation in dynamic coupling and thermodynamic damping for "right" ENSO amplitude simulation in CGCMs for wrong reasons (Bellenger et al., 2014; Karamperidou et al., 2017; Bayr et al., 2018). The periodicity of the mode under different cold tongue strength basic states displays some dependency on these parameter changes as well. The QB periodicity under a strong cold tongue basic state tends to stay largely in the QB range but decreases/increases somewhat when the dynamic coupling and thermodynamic damping increase/decrease (Figure 6.2d). The QQ periodicity under a weak cold tongue basic state increases to a 5- to 6-year range as thermodynamic damping and dynamic coupling weakens (Figure 6.2f). Further work to carefully validate the CZ model against the observed basic state and to obtain best estimates for model parameters is needed to make direct comparisons with observed changes in ENSO behavior. Nevertheless, the results here indicate a significant sensitivity of the leading mode to dynamic coupling and thermodynamic damping. Thus, it is important that models simulate the individual feedbacks correctly in order to faithfully capture both ENSO variance and pattern diversity. The latter still remains a great challenge for state-of-the-art CGCMs, which are known for a cancellation effect between the dynamic coupling and thermodynamic coupling parameters; indeed, many models may simulate an ENSO with realistic growth rate and periodicity, however, due to an incorrect balance of feedbacks (Bellenger et al., 2014; Karamperidou et al., 2017).

The sensitive dependence of the leading ENSO mode on the basic state is conducive for ENSO pattern diversity because relatively small modulations of the basic state by either natural variability or external forcing may give rise to significant changes in ENSO pattern, growth rate, and periodicity. An alternative hypothesis for this ENSO diversity has also been put forward, attributing it to a single oscillatory ENSO mode that undergoes large nonlinear modifications by processes in the atmosphere and ocean (e.g., Choi et al., 2013; Chen & Majda, 2016, 2017; Takahashi et al., 2019). The relatively short length of the observational record may not be adequate to settle this debate at this point. Further examinations of the existence and behavior of ENSO regimes and their great sensitivity to the climate background state, as well as dynamic and thermodynamic coupling in both CZ-type models and comprehensive climate models are needed to advance our understanding and simulation of ENSO complexity.

6.3. RECHARGE OSCILLATOR (RO) AND BJERKNES-WYRTKI-JIN (BWJ) INDEX

Parallel to the advancements in ENSO instability theory, simple conceptual models have been developed that depict ENSO as an oscillatory phenomenon due to the coupled instability envisioned by Bjerknes (1969), Wyrtki (1985), and Cane and Zebiak (1985). The first conceptual model was the delayed oscillator framework (Suarez & Schopf, 1988; Battisti & Hirst, 1989). This delayed oscillator (DO) paradigm was derived based on numerical simulations from intermediate complexity coupled ocean-atmosphere models. The essence of this DO model reflects two basic processes that cause ENSO SSTA to grow and to oscillate, respectively: (i) the coupled positive Bjerknes feedback provides the fundamental growth mechanism, while (ii) wind-driven oceanic Rossby waves and their western boundary reflection into the equatorial Kevin wave give rise to a delayed negative feedback that causes the ENSO phase transition. By realizing that the recharge and discharge of heat content in the equatorial ocean is achieved collectively by the equatorial waves and thus may be better described as an adjustment process instead of an oceanic wave process with a single delay, Jin developed the simple RO paradigm for ENSO (Jin, 1996, 1997a, 1997b)[1]. The RO model captures the coupled oscillatory instability of ENSO explicitly and succinctly in the simplest possible manner with a two-degree freedom dynamical system. The simplicity of the RO paradigm allows for explicit quantifications of both ENSO growth rate and periodicity, which are referred to as the Bjerknes and Wyrtki indices, respectively (Jin et al., 2006; Lu et al., 2018), or collectively as the Bjerknes-Wyrtki-Jin (BWJ) index. In the next subsection, we briefly discuss the key steps of deriving the RO, and the formulations of the BWJ index that encompass all the main processes important for ENSO linear growth rate and periodicity.

[1] *The term* recharge oscillator *was coined by Mark Cane, who suggested it in his review of the papers by Jin (1997a, 1997b).*

Table A Definitions and values of model variables and parameters

Variable/ Parameter	Definition/Default Values
ε_a	Linear dissipation in the atmosphere, ε_a = (2 days)$^{-1}$
u_a, v_a	Zonal and meridional winds in the lower atmosphere layer
$\beta_0 y$	Coriolis parameter at distance y away from the equator
c_a	Propagation speed of atmospheric Kelvin wave, c_a = 60 m s^{-1}
β	Atmospheric heating parameter, β=1.6×10^4 m^2 s^{-2}
$\overline{T}$, $\overline{c}$	Mean SST and atmospheric convergence
T, c	SST and atmospheric convergence anomalies
u, v	Zonal and meridional ocean currents in the upper ocean layers
τ^x,τ^y	Zonal and meridional wind stresses
h	Fluctuations of thermocline depth
H	Reference thermocline depth
S	Percentage of standard mean wind stress during 1980–2000 (see Figure 6.2)
g	Reduced gravity acceleration, $g' = g\frac{\Delta\rho}{\rho}$
$\Delta\rho$	Density difference between the upper and motionless layers
r	Ocean dynamical damping rate, (2.5 years)$^{-1}$
r_s	Dynamical damping rate of the velocity shear, r_s = (2 days)$^{-1}$
w_s	Ocean upwelling, $w_s = H_1\left(\frac{\partial u_1}{\partial x}+\frac{\partial v_1}{\partial y}\right)$
$M(x)$	Heaviside function, $M(x) = \begin{cases} x, x \geq 0 \\ 0, x < 0 \end{cases}$
$\overline{T}_Z$	Mean vertical temperature gradient in the ocean
T_e	Entrainment temperature anomaly
γ	Entrainment efficiency: γ is set to 0.6 instead of 0.75.
α_s	Thermodynamic damping rate, α_s = (125 days)$^{-1}$
$\overline{h}$	Mean thermocline depth along the equator
T_1, b_1, T_2, b_2	Constants controlling the subsurface temperature anomalies, T_1 = 28°C, T_2 = –40°C, b_1 = (80 m)$^{-1}$, b_2 = (33 m)$^{-1}$

6.3.1. The Formulations of the RO Model and the BWJ Index

Motivated by well-defined spatial patterns from both numerical and analytic eigen solutions of ENSO in broad parameter spaces in JN93, Jin (1997a) further reduced these linear ENSO dynamics into two prognostic equations for eastern equatorial Pacific SSTA (T_E) and warm pool thermocline depth anomaly (h_w):

$$\frac{dT_E}{dt} = RT_E + F_1 h_w, \tag{6.1}$$

$$\frac{dh_w}{dt} = -\varepsilon h_w - F_2 T_E. \tag{6.2}$$

Jin et al. (2006) demonstrated using the CZ model that the growth rate of the most unstable ENSO mode in the linear CZ model can be estimated by deriving the approximate but analytical form of the processes that are encompassed in the parameters R and ε. The former includes the six dominant positive and negative feedbacks that determine the growth of eastern Pacific SSTAs. The latter denotes the dynamic adjustment rate of the equatorial warm pool thermocline depth. The linear frequency of the RO can be evaluated as well using all four parameters. Parameter F_1 represents the ocean dynamic feedback from anomalous zonal advection and vertical heat advection associated with the discharge/recharge of equatorial warm pool heat content. Parameter F_2 indicates the efficiency of the recharge/discharge driven by equatorial wind stress anomalies induced by the ENSO SSTA. The complex eigenvalue of the RO can be written as follows:

$$BWJ = \frac{(R-\varepsilon)}{2} + i\sqrt{F_1F_2 - \frac{(R+\varepsilon)^2}{4}}, \tag{6.3}$$

where the real part of the index was referred to as the ENSO Bjerknes stability (BJ) index in Jin et al. (2006), and the imaginary part as the Wyrtki frequency (WF) index in Lu et al. (2018). Together we refer to the complex eigenvalue as the Bjerknes-Wyrtki-Jin (BWJ) index for the ENSO oscillatory instability as it was first derived in its approximate and quasi-analytical formulation in Jin (1997a, 1997b). It has been demonstrated to be useful for understanding and evaluating ENSO's growth rate and periodicity in both reanalysis data and CGCM simulations.

6.3.2. The Derivation of the BWJ Index

For simplicity, we use the Niño-3 index (SSTAs averaged over 5°S–5°N, 150°–90°W) to represent ENSO SST anomalies. The volume-averaged mixed-layer temperature anomaly tendency equation in the Niño-3 region can be written as follows:

$$\frac{\partial\langle T\rangle}{\partial t} = \underbrace{-\left(\langle\overline{u}\partial_x T\rangle + \langle\overline{v}\partial_y T\rangle + \langle\overline{w}\partial_z T\rangle + \langle u\partial_x\overline{T}\rangle + \langle v\partial_y\overline{T}\rangle + \langle w\partial_z\overline{T}\rangle\right)}_{\text{LDH}}$$
$$\underbrace{-\left(\langle u\partial_x T\rangle + \langle v\partial_y T\rangle + \langle w\partial_z T\rangle\right)}_{\text{NDH}} + \underbrace{\langle Q/(\rho_o C_p H)\rangle}_{\text{TDH}} + \underbrace{\langle R\rangle}_{\text{SG}}, \tag{6.4}$$

where u, v, and w are the zonal, meridional, and vertical velocities, T the potential temperature, Q the net surface heat flux into the ocean, H the mixed-layer depth (set to 50m), C_p the specific heat of seawater at constant pressure (set to 3994 J kg^{-1} K^{-1}), and ρ_0 the reference density of seawater (set to 1025 kg m^{-3}). R denotes subgrid-scale processes and overbars denote climatological means. The terms on the right-hand side (RHS) of Eq. (6.4) represent linear dynamic heating (LDH), nonlinear dynamical heating (NDH), thermodynamic heating (TDH), and subgrid-scale contributions (SG) (e.g., oceanic turbulent mixing, nonlinear heating due to tropical instability wave and eddy activity) (An & Jin, 2004).

Following Jin et al. (2006) and also denoting $\langle T\rangle$ as T_{E}, the above equation can then be linearized as follows:

$$\frac{\partial T_{\mathrm{E}}}{\partial t} \approx \underbrace{-\left(\frac{\langle\overline{u}\rangle}{L_x} + \frac{\langle -2y\overline{v}\rangle}{L_y^2} + \gamma\frac{\langle M(\overline{w})\overline{w}\rangle}{H_m}\right)T_{\mathrm{E}}}_{\text{DD}} + \underbrace{\gamma\frac{\langle M(\overline{w})\overline{w}\rangle}{H_m}\langle T_{sub}\rangle}_{\text{TH}}$$
$$\underbrace{-\langle u\rangle\langle\partial_x\overline{T}\rangle}_{\text{ZA}} \underbrace{-\langle v\rangle_A\langle\partial_y\overline{T}\rangle_A}_{\text{MA}} \underbrace{-\langle w\rangle\langle M(\overline{w})\partial_z\overline{T}\rangle}_{\text{VA}} + \underbrace{\langle Q\rangle/(\rho_0 C_p H_m)}_{\text{TD}}. \tag{6.5}$$

The terms on the RHS of Eq. (6.5) represent advection due to mean zonal and meridional currents as well as mean upwelling (also referred to as dynamical damping, DD), the thermocline feedback (TH), the zonal advective feedback (ZA), the meridional advective feedback (MA), the vertical advective feedback (VA), and the thermodynamic damping (TD), respectively. L_x and L_y are the effective zonal and meridional scales that reflect box averaged quantities. The factor y in the second term on the RHS denotes the meridional coordinate, which comes from the assumption that the SSTAs have a Gaussian-like meridional pattern with an e-folding decay (Jin et al., 2006), $M(x) = \begin{cases} 1, & x > 0 \\ 0, & otherwise, \end{cases}$ is a Heaviside step function that only considers regions with upward vertical motion, H_m is the effective depth for the vertical advection (set to 50 m), and T_{sub} is the subsurface temperature at 75 m depth. As for the CZ model (Zebiak & Cane, 1987), the parameter γ (set to 0.75) measures the effectiveness of vertical entrainment using box-averaged quantities to represent the average vertical advection from gridded data. The nonlinear and subgrid terms will be considered in a later subsection.

Following Jin (1997b) and Jin et al. (2006), we give a brief account of the key assumptions for deriving the RO model and the BWJ index using SODA version 3.3.1 reanalysis data (Carton et al., 2018) for the period 1980–2015. The Niño-3 region (5°S–5°N, 150°–90°W) is used to represent ENSO SST variability (Figure 6.4a). The zonal wind response to the positive SSTA shows strong anomalous westerlies in the western and central Pacific and weak anomalous easterlies in the eastern Pacific (Figure 6.4a). This Gill-Matsuno response (Matsuno, 1966; Gill, 1980) delineates the different zonal wind responses to the west and east of the heating source. We use the Sverdrup balance to relate the thermocline anomalies in the western and eastern equatorial box to zonal wind stress anomalies in the central Pacific (Figure 6.4a). Following the CZ model framework, the anomalous upwelling in the eastern Pacific consists of both Ekman upwelling and wave-induced upwelling; the former is related to the local zonal wind stress anomalies, whereas the latter is related to the nonlocal thermocline tendency, which may be further related to warm pool heat content and ENSO SST. The mixed-layer equatorial zonal and meridional currents and upwelling anomalies in the Niño-3 box all have both Ekman and geostrophic components. The Ekman part is determined by the local wind stress in the Niño-3 box, whereas the geostrophic part can be approximately related to remote zonal wind stress in the central Pacific and the thermocline depth in the equatorial Pacific (Jin, 1997b; Jin & An, 1999). Subsurface temperature anomalies in the eastern Pacific are related to the thermocline anomaly locally (Figure 6.4a). Finally, the net thermodynamic heating from surface heat flux anomalies is linearized in

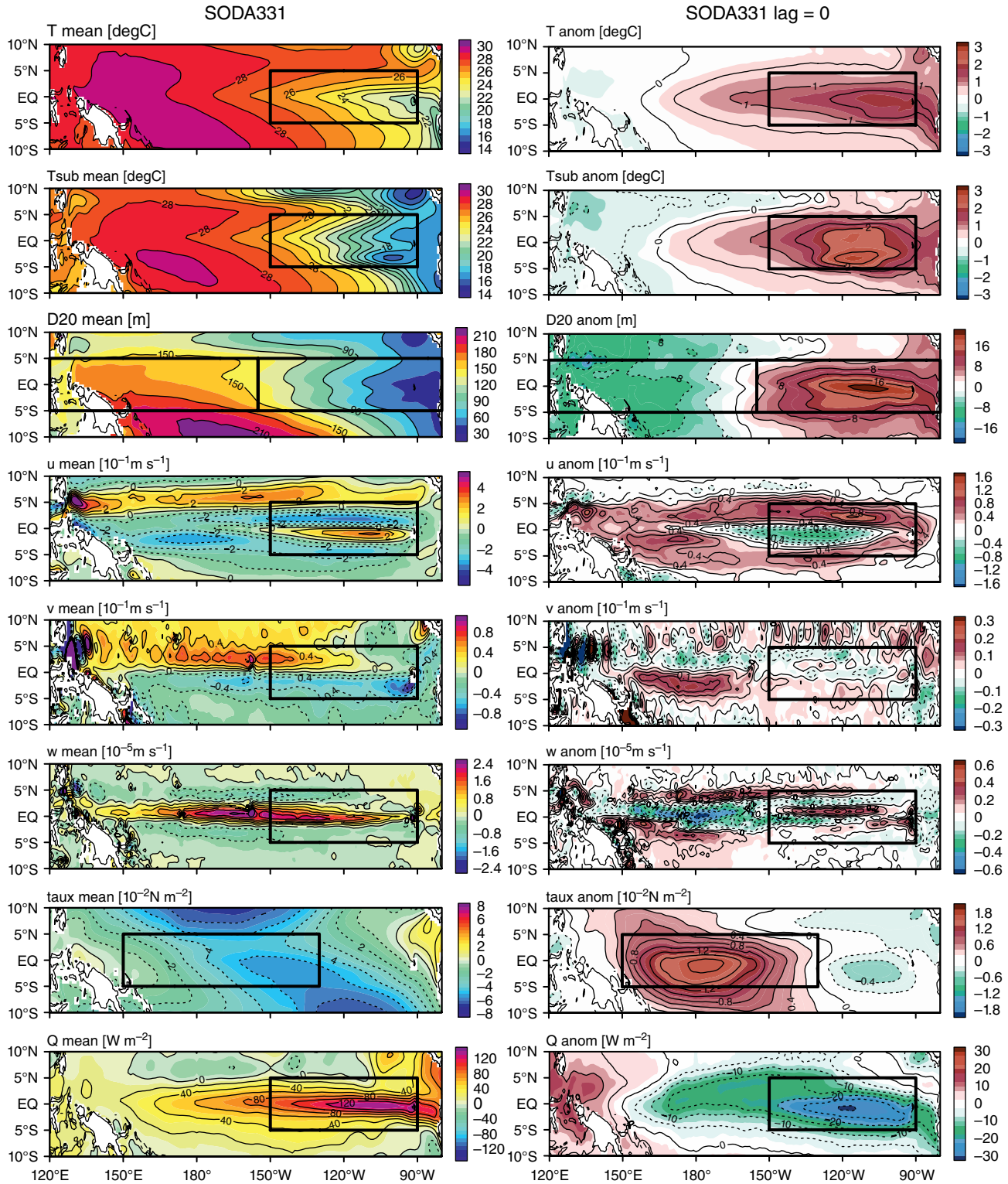

Figure 6.4 Equatorial Pacific annual mean climatology and relevant anomalies during El Niño peak phase. The El Niño peak state is represented by the regressed anomalies onto the normalized volume averaged mixed layer (0–50 m) ocean temperature anomaly over the Niño-3 region. Panels from top to bottom are horizontal distributions of mixed layer temperature, subsurface temperature at 75 m depth, thermocline depth (20°C isotherm depth), mixed layer zonal current, mixed layer meridional current, vertical motion at bottom of mixed layer (at 50 m), zonal wind stress, and net heat flux into the ocean. The Niño-3 region (5°S–5°N, 150°–90°W), h_w (5°S–5°N, 120°E–155°W), h_e (5°S–5°N, 155°–80°W), and $[\tau_x]$ (5°S–5°N, 150°E–130°W) regions are indicated by black boxes.

terms of local SSTA (Figure 6.4a). These quasi-balance approximation linear relationships can be derived from the CZ framework and be expressed as follows:

$$[\tau_x] = \mu_a T_{\mathrm{E}}, \tag{6.6}$$

$$\langle \tau_x \rangle = \mu_a^* T_{\mathrm{E}}, \tag{6.7}$$

$$h_{\mathrm{e}} - h_{\mathrm{w}} = \beta_h [\tau_x], \tag{6.8}$$

$$\langle w \rangle = -\beta_{wr} [\tau_x] - \beta_{wl} \langle \tau_x \rangle + \beta_{wh} h_{\mathrm{w}}, \tag{6.9}$$

$$\langle u \rangle = \beta_{ur} [\tau_x] + \beta_{ul} \langle \tau_x \rangle + \beta_{uh} h_{\mathrm{w}}, \tag{6.10}$$

$$\langle v \rangle_A = \beta_{vr} [\tau_x] + \beta_{vl} \langle \tau_x \rangle + \beta_{vh} h_{\mathrm{w}}, \tag{6.11}$$

$$\langle T_{sub} \rangle = a_h h_{\mathrm{e}}, \tag{6.12}$$

$$\langle Q \rangle / (\rho_0 C_p H) = -\alpha T_{\mathrm{E}}, \tag{6.13}$$

where $[\tau_x]$ denotes central equatorial Pacific zonal wind stress anomalies (5°S–5°N,150°E–130°W), $\langle \tau_x \rangle$ the averaged zonal wind stress anomalies in the Niño-3 region, h_{e} the averaged thermocline depth anomalies over the eastern Pacific box (5°S–5°N,155°–80°W), and h_{w} the averaged thermocline depth anomalies over the western Pacific box (5°S–5°N, 120°E–155°W). By combining Eqs. (6.6) and (6.8), we get the following linear relation:

$$h_{\mathrm{e}} - h_{\mathrm{w}} = \beta_T T_{\mathrm{E}}. \tag{6.14}$$

The feedback coefficients are determined using linear regressions.

Figure 6.5 shows time series and scatter plots of the linear relations in Eqs. (6.6)–(6.13) obtained from SODA reanalysis. The linear balance equation for $[\tau_x]$ holds very well with a correlation coefficient between $[\tau_x]$ and $\mu_a T_{\mathrm{E}}$ of 0.81 (Figure 6.5a). However, the linear relation for $\langle \tau_x \rangle$ is very weak (Figure 6.5b), partly because of its sensitivity to the SSTA pattern according to the Gill-Matsuno response (Gill, 1980). The Sverdrup balance, subsurface temperature anomalies, and surface heat flux anomalies relations hold remarkably well with correlation coefficients of 0.83, 0.97, and 0.87, respectively (Figure 6.5c, g, h). The linear closure relationships for ocean zonal and meridional currents and upwelling are slightly weaker, with correlation coefficients of 0.70, 0.87, and 0.80, respectively (Figure 6.5e, f, d), because of significant uncertainties in ocean current data (Hayashi & Jin, 2017) and oceanic nonlinearities (Dijkstra, 2005). The estimated parameters are listed in Table 6.1.

Using the linear relationships in Eqs. (6.6)–(6.13), those six RHS terms can be expressed linearly in T_{E} and h_{w}, which yields formulations for R and F_1 as follows:

$$\begin{aligned} R = & \underbrace{-\left(\frac{\langle \bar{u} \rangle}{L_x} + \frac{\langle -2y\bar{v} \rangle}{L_y^2} + \gamma \frac{\langle M(\bar{w})\bar{w} \rangle}{H_m} \right)}_{\mathrm{DD}} + \underbrace{\mu_a \beta_h a_h \gamma \frac{\langle M(\bar{w})\bar{w} \rangle}{H_m}}_{\mathrm{TH}} + \\ & \underbrace{(\mu_a \beta_{ur} + \mu_a^* \beta_{ul}) \langle -\partial_x \bar{T} \rangle}_{\mathrm{ZA}} + \underbrace{(\mu_a \beta_{vr} + \mu_a^* \beta_{vl}) \langle -\partial_y \bar{T} \rangle_A}_{\mathrm{MA}} + \\ & \underbrace{(\mu_a \beta_{wr} + \mu_a^* \beta_{wl}) \langle M(\bar{w}) \partial_z \bar{T} \rangle}_{\mathrm{VA}} \underbrace{-\alpha}_{TD}, \end{aligned} \tag{6.15}$$

$$F_1 = \underbrace{\beta_{uh} \langle -\partial_x \bar{T} \rangle}_{\mathrm{ZA}} + \underbrace{\beta_{vh} \langle -\partial_y \bar{T} \rangle_A}_{\mathrm{MA}} \underbrace{- \beta_{wh} \langle M(\bar{w}) \partial_z \bar{T} \rangle}_{\mathrm{VA}} + \underbrace{a_h \gamma \frac{\langle M(\bar{w})\bar{w} \rangle}{H_m}}_{\mathrm{TH}}. \tag{6.16}$$

By considering both Ekman and quasi-balanced wave dynamics induced zonal and meridional current anomalies and upwelling anomalies in Eqs. (6.9)–(6.11), our new formulation established here is more complete in assessing the roles of Ekman feedback than those in Jin et al. (2006), Kim and Jin (2011), and Lu et al. (2018) as it now appears consistently in the zonal, meridional, and vertical advection terms.

Following the equatorial strip approximation to the ocean dynamics equations (Eqs. [3.4]–[3.5] in Jin, 1997b), the slow adjustment of the warm pool ocean heat content described by linear reduced gravity wave ocean dynamics can be further systematically reduced into its simplest possible form as

$$\frac{dh_{\mathrm{w}}}{dt} = -\varepsilon h_{\mathrm{w}} - \kappa [\tau_x] = -\varepsilon h_{\mathrm{w}} - F_2 T_{\mathrm{E}}, \tag{6.17}$$

where $\varepsilon = (1 - r_{\mathrm{w}} r_{\mathrm{e}})C/2L$, $F_2 = \kappa \mu_a$, and $\kappa = (\theta - r_{\mathrm{e}})L/4\rho HC^2$. Here, ε is the slow adjustment scale, which depends on the Kelvin wave speed (C), the Pacific basin width (L), and constant wave reflection efficiencies at the lateral boundaries (r_{w}, r_{e}). Parameter κ is the warm pool ocean heat content recharge/discharge efficiency. It depends on the proportionality of wind stress curl off the equator to the wind stress on the equator (θ), and the eastern boundary reflection efficiency (Jin, 1997b). Equation (6.17) can be solved analytically by presenting heat content information as the integral effect of the finite memory of SSTA, i.e.,

$$\hat{h}_{\mathrm{w}} = -F_2 \int_{-\infty}^{t} e^{\varepsilon(s-t)} T_{\mathrm{E}}(s)\, ds. \tag{6.18}$$

Parameters ε and F_2 depend on the ENSO wind stress pattern, including its meridional width and longitudinal

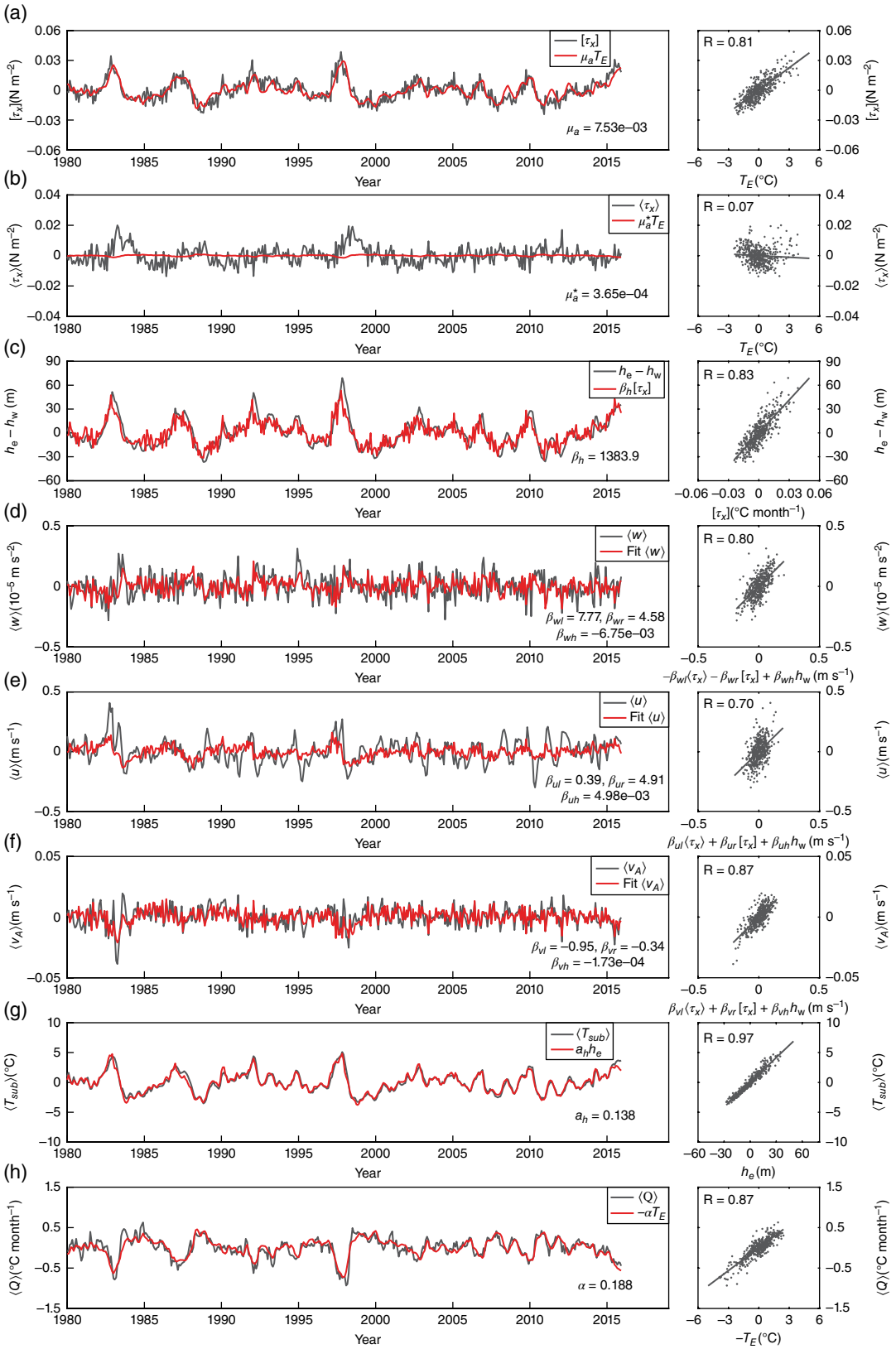

Figure 6.5 Time series (left panels) and scatter plots (right panels) from the balanced relations for deriving and determining the parameters of the recharge oscillator (RO) model. (a) $[\tau_x] = \mu_a T_E$, (b) $\tau_x = \mu_a^* T_E$, (c) $h_e - h_w = \beta_h[\tau_x]$, (d) $\langle w\rangle = -\beta_{wr}[\tau_x] - \beta_{wl}\langle\tau_x\rangle + \beta_{wh}h_w$, (e) $\langle u\rangle = \beta_{ur}[\tau_x] + \beta_{ul}\langle\tau_x\rangle + \beta_{uh}h_w$, (f) $\langle v\rangle_A = \beta_{vr}[\tau_x] + \beta_{vl}\langle\tau_x\rangle + \beta_{vh}h_w$, (g) $\langle T_{sub}\rangle = a_h h_e$, and (h) $\langle Q\rangle/(\rho_0 C_p H) = -\alpha T_E$. The black and red curves denote the observed monthly anomalies and fitted monthly anomalies, respectively. The feedback coefficients and correlation coefficients between observed and fitted anomalies are indicated.

Table 6.1 The annual mean background state parameters, feedback coefficients, and Bjerknes-Wyrtki-Jin index for Niño-3 region estimated using the SODA-3.3.1 monthly data.

Symbol	Value	Unit	Note
H	50	m	Mixed layer depth
L_x	6.67×10^{6}	m	Effective zonal scale
L_y	1.11×10^{6}	m	Effective meridional scale
H_m	50	m	Effective vertical scale for vertical advection
γ	0.75	1	Mixing efficiency of $\langle T\rangle - \langle T_{sub}\rangle$
$\langle\bar{u}\rangle / L_x$	-1.31×10^{-8}	s^{-1}	Scaled mean zonal current
$\langle -2y\bar{v}\rangle / L_y^2$	-1.36×10^{-8}	s^{-1}	Scaled mean meridional current
$\langle M(\bar{w})\bar{w}\rangle / H_m$	7.62×10^{-8}	s^{-1}	Scaled mean upwelling
$\langle \partial_x \bar{T}\rangle$	-5.58×10^{-7}	°C m^{-1}	Zonal gradient of mean temperature
$\langle \partial_y \bar{T}_A\rangle$	4.13×10^{-6}	°C m^{-1}	Antisymmetric competent of meridional gradient of mean temperature
$\langle M(\bar{w})\partial_z \bar{T}\rangle$	4.84×10^{-2}	°C m^{-1}	Vertical gradient of mean temperature
μ_a	7.53×10^{-3}	N m^{-2} °C^{-1}	Eq. (6.6)
μ_a^*	-3.65×10^{-4}	N m^{-2} °C^{-1}	Eq. (6.7)
β_h	1383.9	m^3 N^{-1}	Eq. (6.8)
β_{ur}	4.91	m^3 s^{-1} N^{-1}	Eq. (6.10)
β_{ul}	0.39	m^3 s^{-1} N^{-1}	Eq. (6.10)
β_{uh}	4.98×10^{-3}	s^{-1}	Eq. (6.10)
β_{vr}	-0.34	m^3 s^{-1} N^{-1}	Eq. (6.11)
β_{vl}	-0.95	m^3 s^{-1} N^{-1}	Eq. (6.11)
β_{vh}	-1.73×10^{-4}	s^{-1}	Eq. (6.11)
β_{wr}	4.58×10^{-5}	m^3 s^{-1} N^{-1}	Eq. (6.9)
β_{wl}	7.77×10^{-5}	m^3 s^{-1} N^{-1}	Eq. (6.9)
β_{wh}	-6.75×10^{-8}	m^3 s^{-1} N^{-1}	Eq. (6.9)
a_h	0.138	°C m^{-1}	Eq. (6.12)
α	0.188	$month^{-1}$	Eq. (6.13)
β_T	14.7	m°C^{-1}	Eq. (6.14)
R	0.79	$year^{-1}$	Eq. (6.15)
F_1	0.46	°C m^{-1} $year^{-1}$	Eq. (6.16)
ε	1.40	$year^{-1}$	Eq. (6.18)
F_2	18.2	m °C^{-1} $year^{-1}$	Eq. (6.18)
BJ	-0.30	$year^{-1}$	$(R-\varepsilon)/2$
WJ	2.34	year	$4\pi / \sqrt{4F_1F_2 - (R+\varepsilon)^2}$
WJ_{BF}	2.17	year	$2\pi / \sqrt{F_1F_2}$

location as formulated in Jin (1997b). Here, they are calculated by least square fitting of observed h_w and T_E. Using SODA reanalysis data, this fitting method results in ε = 1.40 $year^{-1}$ and F_2 = 18.2 m °C^{-1} $year^{-1}$, with a correlation coefficient between h_w and $\hat{h}_w$ of ~0.89 (Figure 6.6a).

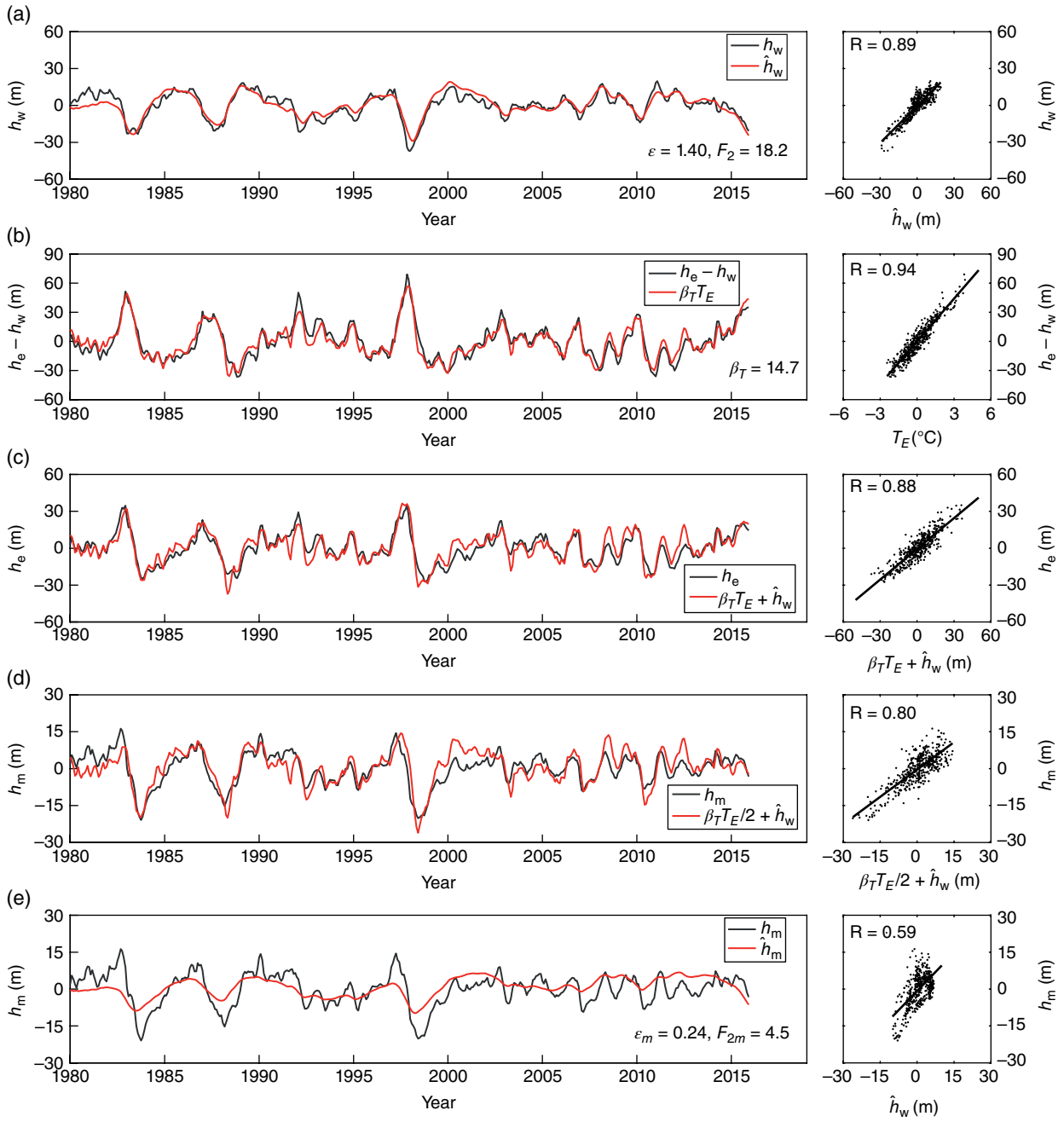

Figure 6.6 Time series (left panels) and scatter plots (right panels) from the thermocline dynamics of the RO model. (a) Western Pacific thermocline depth anomalies h_w and RO $\hat{h}_w$ using Eq. (6.18), (b) thermocline depth tilt $h_e - h_w$ and $\beta_T T_E$, (c) eastern Pacific thermocline depth anomalies h_e and $\beta_T T_E + \hat{h}_w$, (d) basin mean thermocline depth anomalies h_m and $\beta_T T_E / 2 + \hat{h}_w$, (e) same as (d) but for RO fitted $\hat{h}_m$ using Eq. (6.20). The feedback coefficients and correlation coefficients between observed and fitted anomalies are indicated.

Warm pool heat content discharge and equatorial wide heat content discharge (h_m) are related (Wyrtki, 1985; Jin, 1997a, 1997b):

$$h_m = (h_e + h_w)/2 \approx \beta_T T_E / 2 - F_2 \int_{-\infty}^{t} e^{\varepsilon(s-t)} T_E(s)\, ds. \qquad (6.19)$$

The above expression for basinwide heat content is similar to Eq. (8.7) of Fedorov (2010), who derived a slightly more complex formulation also using both Sverdrup balance and a slow oceanic adjustment process under a weak oceanic damping assumption. As shown in Figure 6.6a–d, the slow ocean heat content adjustment and equatorial Sverdrup balance capture the relation of ENSO SST with western, eastern, and zonal mean equatorial heat content remarkably well, with improved correlations compared to previous studies (Fedorov, 2010; Izumo et al., 2019).

Both warm pool heat content and basinwide heat content have been used in the past to describe the recharge/discharge process (Jin, 1997a; Lu et al., 2018). In order to test which one is more suitable, we use a similar form of Eq. (6.2) but with two different parameters for basinwide heat content:

$$\hat{h}_{\mathrm{m}} = -F_{2\mathrm{m}} \int_{-\infty}^{t} e^{\varepsilon_{\mathrm{m}}(s-t)} T_{\mathrm{E}}(s) ds \tag{6.20}$$

The best fit gives an adjustment time scale of 0.24 year^{-1}, which is much longer than that for western equatorial heat content. This is consistent with the notion that equatorial heat content has a slow adjustment time scale (Burgers et al., 2005). However, the resulting $\hat{h}_{\mathrm{m}}$ only captures the very slow variation of h_{m} with a correlation coefficient of about 0.59 (Figure 6.6e), which is a significantly less effective expression for equatorial heat content than the expression that combines the Sverdrup balance and the western Pacific warm-pool heat content (Eq. 6.19). This result is consistent with recent studies (Neske & McGregor, 2018; Planton et al., 2018; Izumo et al., 2019), suggesting that western equatorial heat content is better suited to describe the recharge/discharge process.

With these analytical formulations of ε and F_2, we now derive all the parameters in the BWJ index for the RO under a number of reasonable quasi-balance approximations. For the SODA reanalysis mean state, the BWJ index yields an ENSO growth rate of −0.30 year^{-1} and a period of 2.34 years (Table 6.1), which indicates that ENSO linear coupled dynamics are very close to criticality. This is significantly different from a much stronger damping rate estimated from linear inverse modeling. This difference largely comes from the fact that the nonlinear damping from both deterministic and stochastic nonlinear processes are already included in the estimated ENSO growth rate from linear inverse modeling by construction but not included in the BWJ index. Furthermore, the estimated linear period is substantially shorter than the average observed ENSO period. This periodicity is sensitive to the characterization of the basic state, the details of parameterizing the subsurface temperature anomalies, and the nonlinear corrections (see the appendix of Jin, 1997a). Nevertheless, this linear analysis of the BWJ index is roughly consistent with fitting the linear RO model directly with observational data, although the latter method gives a more negative linear growth rate but longer period. The advantage of using the BWJ index comes from its decomposition of the contributions to ENSO growth rate and frequency from different coupled processes. As shown in Figure 6.7a, the TH feedback is the largest contributor to the instability growth, and the ZA feedback is the second largest. The TD damping is the largest damping term and the DD the second largest. These results are consistent with the results obtained from the SODA 2.0.2 reanalysis (Kim et al., 2014).

6.3.3. Seasonal Modulation of BWJ Index

In this subsection, we consider seasonal modulations of the RO due to seasonality in the background state and feedback coefficients. As shown in Figure 6.7b, seasonality in the Sverdrup balance, i.e., the response of the thermocline in the western equatorial Pacific to central Pacific wind stress anomalies (β_h), has a positive TH feedback maximum during boreal winter and a minimum during late spring and summer. The seasonal response of thermodynamic heating to local SST (α) results in a negative TD feedback that has its maximum during late winter and spring and a minimum during fall. Seasonality in the strength of the mean ocean currents results in a negative MA feedback maximum during spring and a minimum during late summer and fall. The seasonal strength of zonal and meridional advection feedbacks results in a positive ZA feedback maximum during fall and a minimum during late winter and spring. The joint effect is a seasonal growth rate that is maximum during boreal late summer and minimum during spring, consistent with the results of Stein et al. (2014). The seasonal processes described have been noted to play an important role both in the seasonal synchronization of ENSO (Stein et al., 2014) and the ENSO spring auto-correlation barrier (Levine & McPhaden, 2016). There is also strong seasonality in the Wyrtki index, although the actual impact of seasonality on ENSO main periodicity should be properly assessed using the Floquet exponent analysis (Jin et al., 1996). Additional discussion of ENSO seasonality is given in section 6.4.

6.3.4. Nonlinear Dynamical Heating, Subgrid Processes, and Noise Forcing of ENSO

Next, we decompose the SSTA equation as

$$\frac{\partial T_{\mathrm{E}}}{\partial t} = \left[\frac{\partial T_{\mathrm{E}}}{\partial t}\right]_{\mathrm{D}} + \left[\frac{\partial T_{\mathrm{E}}}{\partial t}\right]_{\mathrm{N}} = LD + LN + TD + TN + ND + NN + SGD + SGN, \tag{6.21}$$

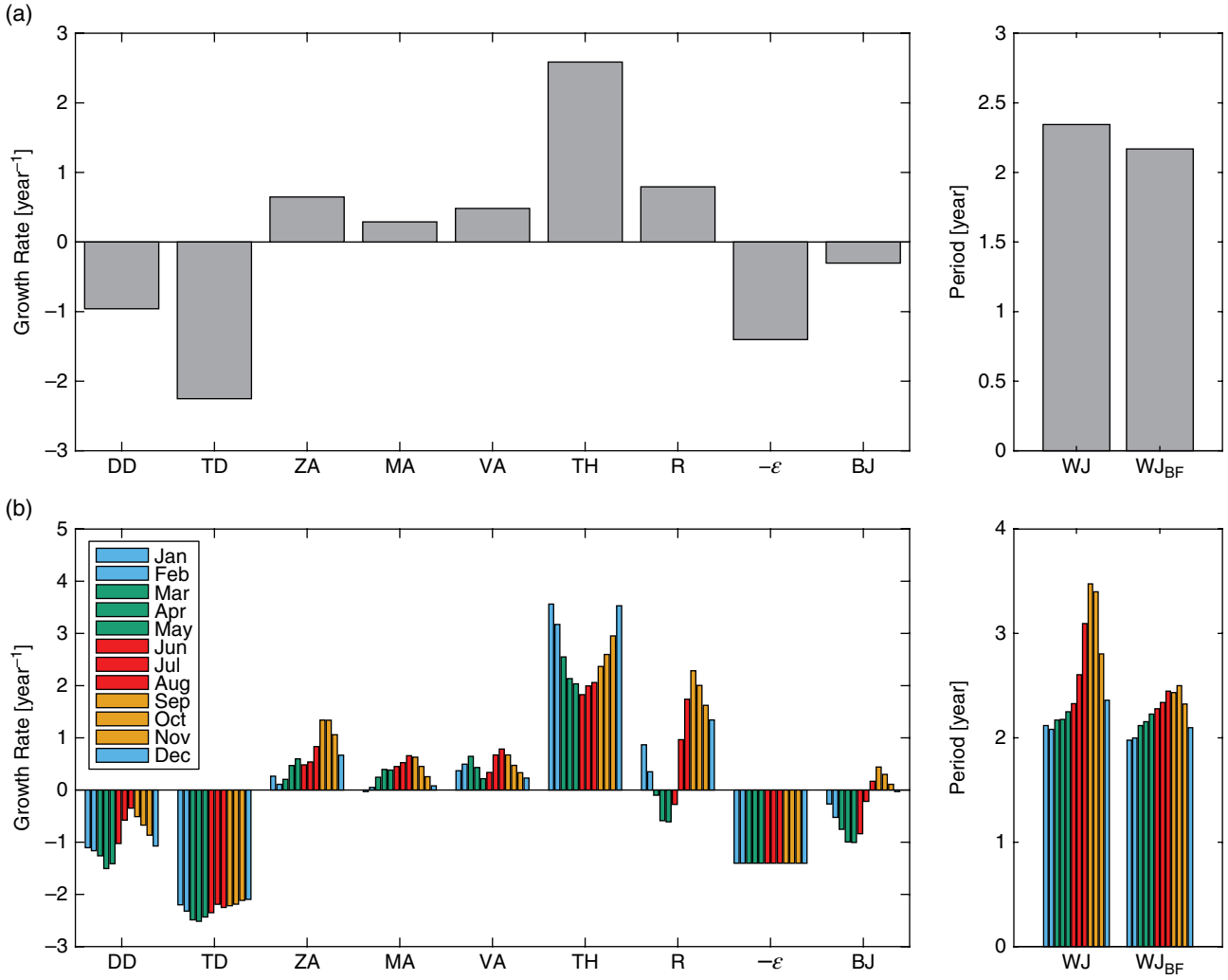

Figure 6.7 The Bjierknes-Wyrtki-Jin index and its individual components. (a) The estimates using the annual mean background state and feedback coefficients derived from monthly data. (b) The estimates using each month background state and feedback coefficients derived from data for each month. DD represents the dynamic damping, TD the thermodynamic damping, ZA the zonal advective feedback, MA the meridional advective feedback, VA the vertical advection feedback, TH the thermocline feedback, R = MA+TD+ZA+YA+TH+EK, ε represents dynamic adjustment rate of the equatorial warm-pool thermocline depth, BJ is the Bjerknes stability index (R-ε)/2, WJ represents Wyrtki period index, and WJ_{BF} is the period index ignoring contributions of R and ε, i.e., $2\pi / \sqrt{F_1 F_2}$.

where $\left[\frac{\partial T_E}{\partial t}\right]_D$ and $\left[\frac{\partial T_E}{\partial t}\right]_N$ denote the total deterministic feedbacks and noise, LD and LN denote linear dynamic deterministic feedbacks and noise, TD and TN denote thermodynamic deterministic feedback and noise, ND and NN denote nonlinear dynamic deterministic terms and noise, and SGD and SGN denote subgrid dynamic deterministic terms and noise, respectively. Based on the RO framework, the linear deterministic terms can be written as

$$LD = (\mathrm{R} + \alpha) T_E + F_1 h_w, \tag{6.22}$$

$$TD = -\alpha T_E. \tag{6.23}$$

$$ND = C_{N1} T_E^2 + C_{N2} T_E h_w + C_{N3} T_E^3 + C_{N4} T_E^2 h_w + C_{N5} T_E h_w^2, \tag{6.24}$$

$$SGD = C_{S1} T_E + C_{S2} h_w + C_{S3} T_E^2 + C_{S4} T_E h_w + C_{S5} T_E^3 + C_{S6} T_E^2 h_w + C_{S7} T_E h_w^2. \tag{6.25}$$

The oceanic mixing and subgrid feedbacks included in the residual contribute to the linear feedbacks. This calls for a more thorough study of how these processes contribute to basic ENSO dynamics. Moreover, by fitting the NDH and SG with the form of Eqs. (6.24) and (6.25), we note that there are three cubic and two quadratic nonlinear terms that tend to dominate the ND and SGD terms. The coefficients are listed in Tables 6.2 and 6.3. This finding suggests that the nonlinear deterministic dynamics and nonlinearity from the subgrid processes may both contribute to the nonlinearity of ENSO.

As shown in Figure 6.8, we find a correlation coefficient of R(LD, LDH) = 0.57. The thermodynamic term is captured remarkably well with a correlation coefficient of R(TD, TDH) = 0.87. By least square fitting NDH using Eq. (6.24), we find a correlation of R(ND, NDH) = 0.55, and by least square fitting SG using Eq. (6.25), we find a correlation of R(SGD, SG) = 0.49. The nonlinear terms, particularly the substantial cubic nonlinear terms, serve as nonlinear damping, whereas the relative weak quadratic nonlinear terms may contribute to ENSO asymmetry, all of which will be demonstrated in section 6.4.

Similarly, we decompose the warm pool thermocline depth equation into the deterministic and noise terms as

$$\frac{\partial h_{\mathrm{w}}}{\partial t} = \left[\frac{\partial h_{\mathrm{w}}}{\partial t}\right]_{\mathrm{D}} + \left[\frac{\partial h_{\mathrm{w}}}{\partial t}\right]_{\mathrm{N}}, \tag{6.26}$$

where the deterministic part can be written as

$$\left[\frac{\partial h_{\mathrm{w}}}{\partial t}\right]_{\mathrm{D}} = -\varepsilon h_{\mathrm{w}} - F_2 T_{\mathrm{E}}. \tag{6.27}$$

In addition to the linear and nonlinear deterministic dynamics, we can also assess the noise forcing terms:

$$\mathrm{LN} = \mathrm{LDH} - \mathrm{LD}, \tag{6.28}$$

$$\mathrm{TN} = \mathrm{TDH} - \mathrm{TD}, \tag{6.29}$$

$$\mathrm{NN} = \mathrm{NDH} - \mathrm{ND} \tag{6.30}$$

$$\mathrm{SGN} = \mathrm{SG} - \mathrm{SGD}. \tag{6.31}$$

It is clear that the total noise forcing has considerable amplitude on time scales much faster than the ENSO time scale. However, this high-frequency noise forcing estimated in this low-order system is not at all effective in exciting low-frequency (i.e., interannual) ENSO variability. Only the low-frequency part of the noise forcing can effectively drive ENSO and thereby affect ENSO amplitude. It is also worthy to mention that when the low-frequency component of the noise is truly a part of near white noise, it has no predictability, Therefore, the predictability of ENSO largely resides in its linear and nonlinear deterministic dynamics.

Figure 6.9 illustrates the linear, nonlinear, and noise forcing tendency vectors in RO phase space. The rotation and divergence of vectors demonstrate the oscillator and growth of ENSO. As shown in Figure 6.9, the linear deterministic vectors demonstrate an obvious clockwise rotation. In contrast, the rotation signal over the nonlinear deterministic and noise forcing tendency vectors are less clear; this indicates that ENSO oscillation is dominated by linear deterministic dynamics.

6.3.5. On the Relationship of the RO and DO Paradigms

The DO and RO models for ENSO have been considered as two different but equivalent conceptual models for the basic dynamics of ENSO (Jin, 1997b; Fedorov, 2010). Both models are derived from the CZ framework. The only key difference between the two resides in the consideration of how the equatorial warm pool heat content or the thermocline respond to ENSO wind forcing. In the RO model, the warm pool heat content is governed by adjustment equation (6.13) with its adjustment time scale controlled by both eastern and western boundary reflections, wave propagation time scale, and the mass discharge/recharge due to the near-equatorial

Table 6.2 The coefficients of nonlinear deterministic quadratic and cubic terms.

Symbol	Value	Unit	Terms
C_{N1}	$3.68 + 21.61 \cos \omega_a t - 3.99 \sin \omega_a t$	10^{-2} °C^{-1} year^{-1}	T_E^2
C_{N2}	$-1.48 + 0.83 \cos \omega_a t - 0.56 \sin \omega_a t$	10^{-2} m^{-1} year^{-1}	$T_E h_w$
C_{N3}	$-27.67 - 2.93 \cos \omega_a t - 7.37 \sin \omega_a t$	10^{-2} °C^{-2} year^{-1}	T_E^3
C_{N4}	$-5.01 - 0.69 \cos \omega_a t + 1.43 \sin \omega_a t$	10^{-2} °C^{-1} m^{-1} year^{-1}	$T_E^2 h_w$
C_{N5}	$-0.41 + 0.07 \cos \omega_a t + 0.33 \sin \omega_a t$	10^{-2} m^{-2} year^{-1}	$T_E h_w^2$

Note. ω_a is the annual frequency.

Table 6.3 The coefficients of subgrid deterministic linear, quadratic, and cubic terms.

Symbol	Value	Unit	Terms
C_{S1}	$1.37 + 0.42 \cos \omega_a t + 0.31 \sin \omega_a t$	$year^{-1}$	T_E
C_{S2}	$-3.42 + 2.82 \cos \omega_a t - 1.15 \sin \omega_a t$	10^{-2} °C m^{-1} $year^{-1}$	h_w
C_{S3}	$-26.69 - 12.41 \cos \omega_a t + 34.56 \sin \omega_a t$	10^{-2} °C^{-1} $year^{-1}$	T_E^2
C_{S4}	$-14.79 + 14.99 \cos \omega_a t + 1.25 \sin \omega_a t$	10^{-2} m^{-1} $year^{-1}$	$T_E h_w$
C_{S5}	$-0.14 + 0.69 \cos \omega_a t - 0.30 \sin \omega_a t$	10^{-2} °C^{-2} $year^{-1}$	T_E^3
C_{S6}	$4.64 - 0.42 \cos \omega_a t + 6.75 \sin \omega_a t$	10^{-2} °C^{-1} m^{-1} $year^{-1}$	$T_E^2 h_w$
C_{S7}	$-0.19 + 0.57 \cos \omega_a t + 0.58 \sin \omega_a t$	10^{-2} m^{-2} $year^{-1}$	$T_E h_w^2$

Note. ω_a is the annual frequency.

wind stress curl and wind stress longitudinal location (Jin, 1997b). In contrast, the DO as formulated in Battisti and Hirst (1989) assumed in an ad hoc way that ENSO-induced equatorial wind anomalies in the central Pacific drive an equatorial Rossby wave response that is reflected into an equatorial Kelvin wave and determines the western equatorial thermocline depth without any consideration of eastern boundary reflection, leading to the following simple equation:

$$h_w = -a_w \tau_C (t - \eta). \tag{6.32}$$

There are two parameters in each model. The adjustment time scale and recharge/discharge efficiency in the RO model can both be systematically derived as shown in Jin (1997b). Both the adjustment dynamics formulation (RO) and the delayed response formulation (DO) are of comparable effectiveness in capturing the warm pool heat content evolution to a large extent, but adjustment dynamics not only consider the wind stress curl effect explicitly, but also filter out high frequency noise in the wind stress forcing effectively. In contrast, the delayed response dynamics are less clear on the role of wind stress curl and cannot filter out noise in the wind stress. Moreover, the DO formulation is in fact a more complex mathematical description than the RO formulation because the DO has an infinite number of degrees of freedom in terms of independent eigenmodes, whereas the RO has a minimal two degrees of freedom without redundancy. Nevertheless, conceptually the DO and RO are two succinct descriptions of ENSO basic dynamics, and both have played important roles in advancing ENSO theory. An obvious advantage that stems from the simplicity of the RO paradigm is an algebraic formulation for the BWJ index, which serves as a useful tool for dynamically assessing the various contributions of coupled processes to ENSO linear growth rate and frequency as envisioned by Bjerknes (1969), Wyrtki (1985), and Cane and Zebiak (1985). Further analyses of the phase diagrams and vector fields associated with the simple RO paradigm as shown in Figure 6.9 (also Jin, 1997a; Takahashi et al., 2019) reveal its value in understanding the observed, simulated, and predicted ENSO behaviors.

6.4. FACTORS CONTROLLING ENSO AMPLITUDE, PERIODICITY, PHASE-LOCKING, ASYMMETRY, AND NONLINEAR RECTIFICATION

Sections 6.2 and 6.3 provide a simple account of how the dynamics of the Pacific warm pool and cold tongue basic states allow perturbations to grow into ENSO cycles, and how it largely can be reduced into a minimal RO model for the simplest possible explicit depiction of the Bjerknes-Wyrtki coupled instability for ENSO. In this section, we will use the RO model to systematically revisit basic questions of ENSO dynamics, i.e., what are the key factors that control ENSO amplitude, phase-locking, El Niño/La Niña asymmetry, and its nonlinear rectification onto the mean state.

6.4.1. ENSO Amplitude

To investigate these issues, we consider the following form of the RO model:

$$\frac{dT_E}{dt} = RT_E + \omega_0 h_w + \sigma\xi(1 + BT_E) - cT_E^3 + bT_E^2 \tag{6.33}$$

$$\frac{dh_w}{dt} = -\varepsilon h_w - \omega_0 T_E \tag{6.34}$$

$$\frac{d\xi}{dt} = -m\xi + w(t) \tag{6.35}$$

$$R = R_0 - R_a \sin(\omega_a t - \varphi). \tag{6.36}$$

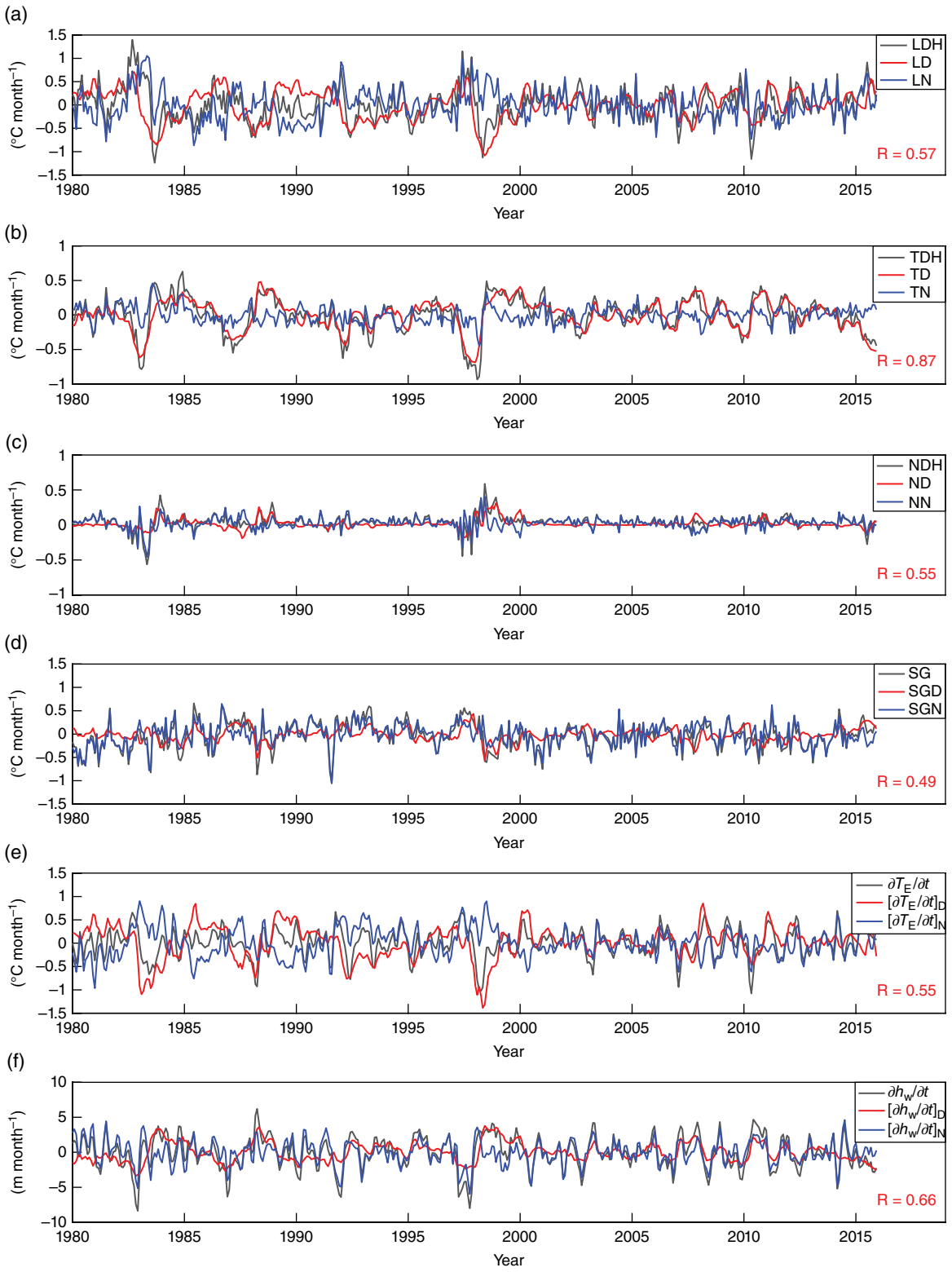

Figure 6.8 Time series of linear and nonlinear deterministic dynamics and noise forcing of the RO model. (a) Linear dynamic T_E tendency and its deterministic part and noise (LDH, LD, and LN, respectively); (b) thermodynamic T_E tendency and its deterministic part and noise (TDH, TD, and TN, respectively); (c) nonlinear dynamic T_E tendency and its deterministic part and noise (NDH, ND and NN, respectively); (d) sub-grid terms of T_E tendency and its deterministic part and noise (SG, SGD, and SGN, respectively); (e) total T_E tendency and its deterministic part and noise; (f) total h_w tendency and its deterministic part and noise. Black curves denote original tendency of LDH, TDH, NDH, SG, $\partial T_E/\partial t$, and $\partial h_w/\partial t$. Red curves denote RO deterministic parts of LD, TD, ND, SGD, $[\partial T_E/\partial t]_D$, and $[\partial h_w/\partial t]_D$. Blue curves denote noise parts of LN, TN, NN, SGN, $[\partial T_E/\partial t]_N$, and $[\partial h_w/\partial t]_N$. The correlation coefficient between deterministic part and original term is indicated, respectively.

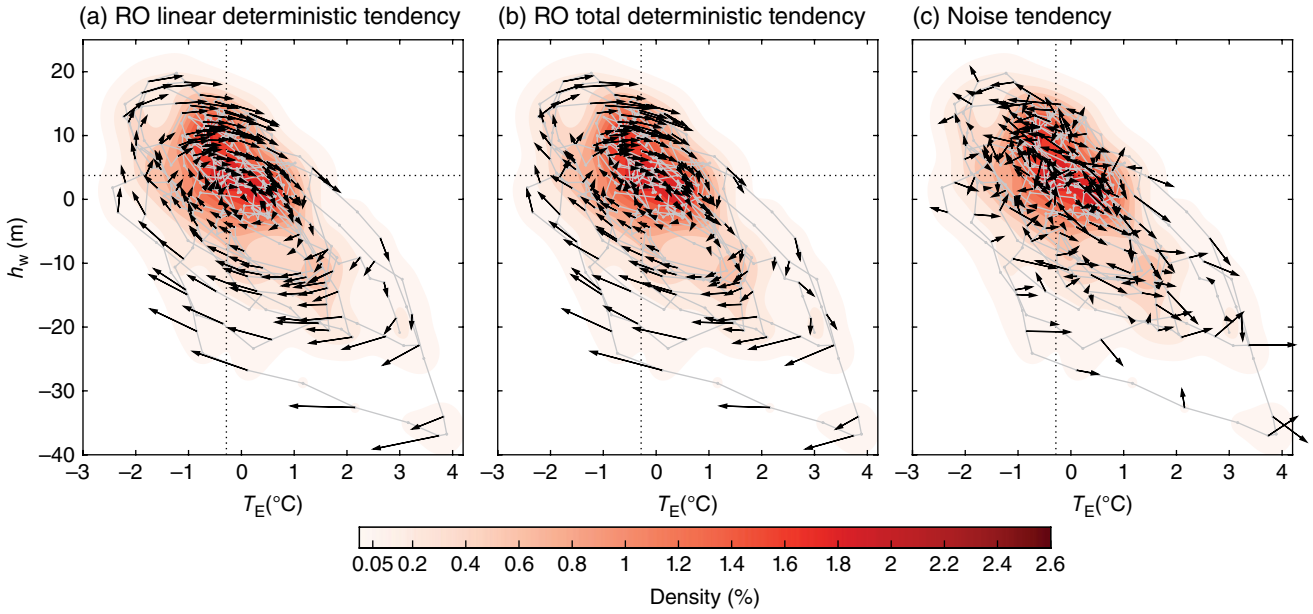

Figure 6.9 Schematic representation of RO linear deterministic, total deterministic, and noise-forcing dynamics. The vectors denote the tendency in phase space of the mixed layer volume averaged temperature anomalies over the Niño-3 region and western Pacific 20°C isotherm depth anomalies (5°S–5°N, 120°E–155°W): (a) (LD+TD, $[\partial h_w/\partial t]_D$), (b) ($[\partial T_E/\partial t]_D$, $[\partial h_w/\partial t]_D$), and (c) ($[\partial T_E/\partial t]_N$, $[\partial h_w/\partial t]_N$), respectively. In the temperature equation, LD and LN denote linear dynamic deterministic feedbacks and noise, TD and TN thermodynamic deterministic feedback and noise, $[\partial T_E/\partial t]_D$ and $[\partial T_E/\partial t]_N$ total deterministic feedbacks and noise, respectively. In thermocline depth equation, $[\partial h_w/\partial t]_D$ and $[\partial h_w/\partial t]_N$ denote linear dynamic deterministic feedbacks and noise, respectively. The shading denotes a kernel density estimate of the joint probability distribution of the two time series, T_E and h_w. The vertical and horizontal dashed lines denote the peak of the probability distribution for T_E and h_w, respectively.

Here, a few additional parameters are introduced for the strength (R_a), frequency (ω_a), and phase (φ) of a seasonal cycle modulation of the growth rate, for cubic (c) and quadratic (b) nonlinearities, and for additive (σ) and multiplicative (σB) noises. Westerly wind bursts (WWBs) affect ENSO, and importantly ENSO also modulates WWBs (e.g., Kessler et al., 1995; Kleeman & Moore,1997; Vecchi & Harrison 2000; Yu et al., 2003; Fedorov et al., 2003, Lengaigne et al., 2004; McPhaden, 2004; Zavala-Garay et al., 2005; Eisenman et al., 2005). The state-dependent stochastic forcing excitations included in the RO model here thus represent ENSO-modulated WWBs (Jin et al., 2007; Levine & Jin, 2010). The quadratic and cubic nonlinearities represent NDH from both deterministic nonlinear advection and upwelling as well as from the upscale effect of ENSO's modulation of tropical instability waves (TIW) (An, 2008; Boucharel & Jin, 2020). One may also include a convective threshold that is nonlinear in the growth rate (Choi et al., 2013; Takahashi et al., 2019). These physically motivated nonlinearities are similar in terms of their qualitative impacts on the basic ENSO properties. As shown in section 6.3, there are a few more nonlinear terms, but the details of how many of these terms are required to model ENSO realistically may vary depending on whether reanalysis data or CGCM simulations are investigated. Here, we will keep the minimum number of nonlinear terms in the nonlinear stochastically forced RO model that is adequate to qualitatively explore the aforementioned fundamental ENSO dynamics.

For simplicity, we first consider a case in which the symmetry breaking processes are disabled ($b = 0$, $B = 0$). We also assume no seasonal cycle modulation ($R_a = 0$), resulting in a base case of the RO model under normal (cubic) nonlinearity and additive noise forcing. By considering a second order closure approximation (e.g., Launder et al., 1975), the fourth moments of SSTA and of the warm pool thermocline anomaly covariability can be expressed in terms of their second moments:

$$\left\langle T_E^{\,4}\right\rangle = K_0\left\langle T_E^{\,2}\right\rangle^2, \left\langle hT_E\right\rangle^3 = K_1\left\langle hT_E\right\rangle\left\langle T_E^{\,2}\right\rangle. \quad (6.37)$$

We can then derive an approximate ENSO SSTA variance equation as follows:

$$\left(R-\varepsilon+\delta\right)\left\langle T_{\mathrm{E}}{}^{2}\right\rangle-\mathrm{c}K_{0}\left\langle T_{\mathrm{E}}{}^{2}\right\rangle^{2}+\hat{\sigma}^{2}=0. \qquad (6.38)$$

Here $\delta \approx \dfrac{\varepsilon^{2}\left(\varepsilon-R-\dfrac{cK_{1}\left\langle T_{\mathrm{E}}{}^{2}\right\rangle}{\varepsilon}\right)}{\omega_{0}^{2}+\varepsilon^{2}-\varepsilon R+cK_{1}\left\langle T_{\mathrm{E}}{}^{2}\right\rangle}$ is a relatively small factor with weak dependence on the ENSO amplitude. This equation clearly indicates that ENSO amplitude depends on only three key factors: (i) the degree of near criticality as measured by the linear growth rate $\left(\dfrac{R-\varepsilon}{2}\right)$, (ii) the strength of cubic nonlinear damping (c), and (iii) the amplitude of stochastic excitation ($\hat{\sigma}^{2}$) as shown in Figure 6.10. How ENSO amplitude depends on the linear growth rate for different levels of noise forcing is shown in Figure 6.10b. When there is no stochastic excitation ($\hat{\sigma}^{2}=0$) (red curve), we have the standard form of ENSO amplitude dependence on criticality with zero self-sustained amplitude that is subcritical ($R-\varepsilon<0$), which is also referred to as stable regime, and a square root dependence of amplitude on the super-criticality ($R-\varepsilon>0$). This result is similar to the solution obtained in the appendix of Jin (1997b). When $\hat{\sigma}^{2}>0$, the stochastically forced solution transforms smoothly into a nonlinear dependence of ENSO amplitude on the criticality. Moreover, the increased level of noise indicates the distribution of ENSO's probability density function becomes flatter (Figure 6.10a). ENSO amplitude decreases significantly when cubic nonlinear damping is increased (Figure 6.10c) in the super-criticality regime ($R-\varepsilon>0$), but less so in the stable ($R-\varepsilon<0$) and near-stable regimes ($R-\varepsilon\le 0$).

We now examine how ENSO amplitude changes in the presence of the three omitted processes, i.e., (i) the seasonal cycle modulation of the growth rate, (ii) the state-dependent noise forcing, and (iii) the quadratic nonlinearity. By solving the ensemble mean equations of the second moment equations using the perturbation method, one may obtain approximate analytical solutions for how ENSO amplitude depends on the three parameters that measure these processes. We find only a weak dependence of ENSO amplitude on the strength of the annual modulation of ENSO growth rate. The state-dependent noise excitation results in a so-called noised-induced destabilization of ENSO to enhance its variance (Jin et al., 2007). This is consistent with a weak increase of ENSO amplitude as parameter B increases. Similarly, quadratic nonlinearity also tends to have a weak impact on ENSO amplitude. Both the quadratic nonlinearity and state-dependent noise excitation are the two main sources for ENSO symmetry breaking, because they affect ENSO warm and cold phases differentially and thus generate ENSO asymmetry. This subject will be discussed briefly in subsection 6.4.3 and more comprehensively in chapter 7.

In summary, the key factors that control ENSO amplitude are (i) the linear growth rate, (ii) the amplitude of the stochastic forcing, and (iii) the amplitude of the cubic nonlinear damping. Other processes, including the seasonal modulation of the growth rate and symmetry breaking processes, are of secondary importance in controlling ENSO amplitude. This insight from simple dynamical theory may provide a useful framework for understanding ENSO amplitude changes in past, present, and future climates both in observational and proxy records, as well as in climate model simulations.

6.4.2. ENSO Phase Locking and Seasonal Modulation of Variance

El Niño and La Niña events tend to peak at the end of the calendar year, a phenomenon called ENSO phase locking. This phase locking is another fundamental ENSO property that is determined by its basic dynamics. It was realized early on that the seasonal cycle of the climate background state can modulate ENSO and cause it to peak in boreal winter. Jin et al. (1996) showed that the seasonal cycle in the cold tongue region alone can give rise to ENSO's phase locking to winter. Tziperman et al. (1997, 1998) and Neelin et al. (2000) further examined different physical processes contributing to ENSO phase locking. Later, the crucial role of the seasonal migration of the warm pool in shifting the equatorial wind response to the Southern Hemisphere and thereby accelerating El Niño termination and contributing to ENSO phase locking was recognized (Vecchi & Harrison, 2006; McGregor et al., 2012; Stuecker et al., 2013). Related, it was suggested that the anomalous low-level anticyclone in the western North Pacific (WNPAC) that develops in late fall to winter during El Niño conditions causes easterly wind anomalies on the equator that result in El Niño termination (Wang et al., 1999). Stuecker et al. (2013, 2015a, 2015b) found that the seasonal-paced southward migration of El Niño-associated westerly wind anomalies and the WNPAC are both part of the so-called ENSO combination mode (C-mode), which is generated by the warm pool seasonal cycle modulation of the atmospheric wind response to ENSO SSTA. As the ENSO C-mode is responsible for the WNPAC genesis, it is fundamentally important to establish ENSO's impacts on the East Asian monsoon system (Stuecker et al., 2015a, 2015b), which is addressed in more detail in chapter 14. Whether ENSO phase locking is predominantly controlled by the seasonal cycle in the warm pool or the cold tongue region is still an unsolved question; however, it is becoming clear that the modulation of the ENSO growth rate is

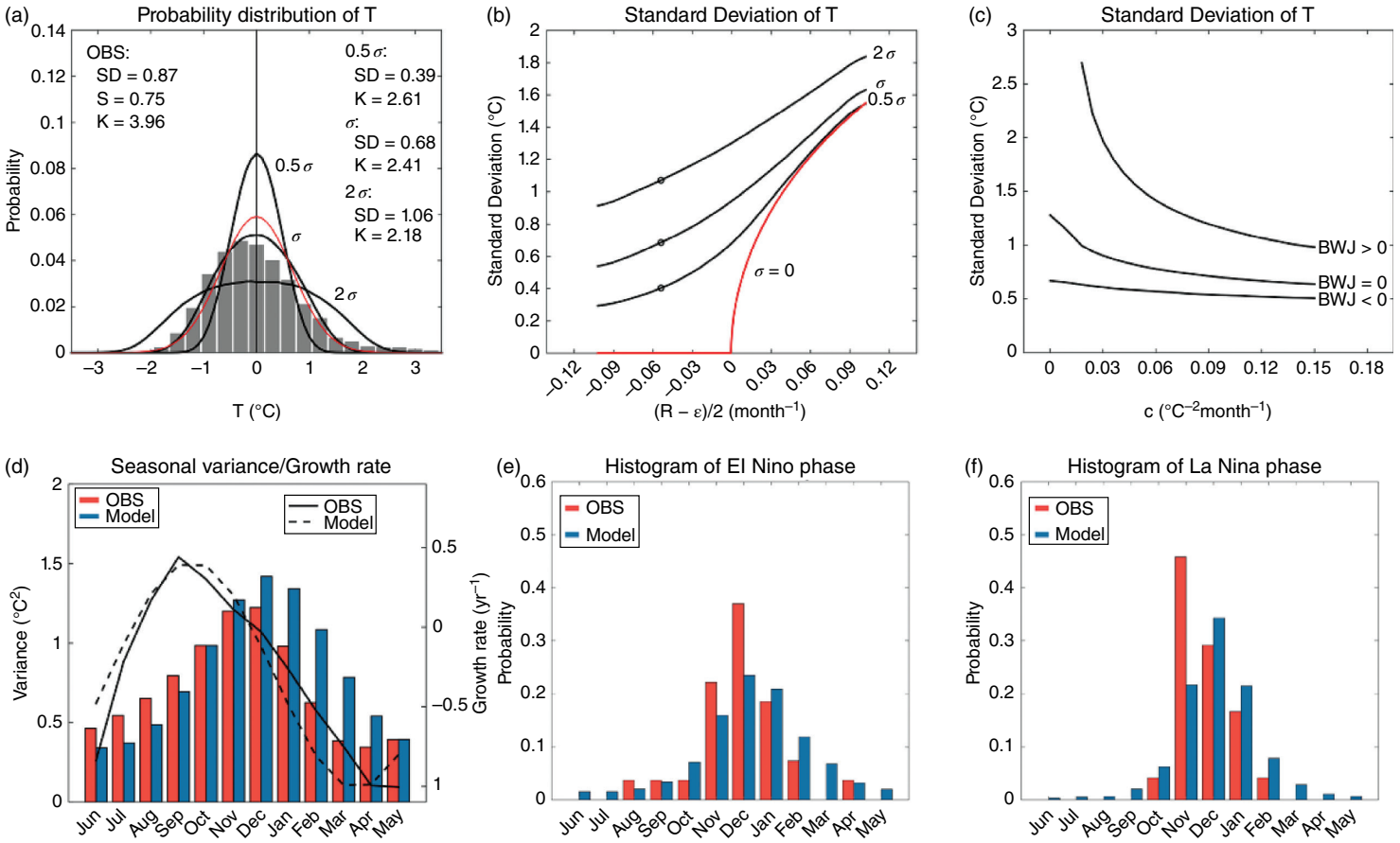

Figure 6.10 (a) Probability distribution of temperature for the observations (gray bar) as well as the model with default, double, and half amplitude of stochastic forcing (black curves). The red curve indicates a Gaussian distribution with standard deviation of the default stochastic forcing amplitude. (b) ENSO amplitude dependence on linear growth for different levels of noise. Circles represent the corresponding results in (a). (c) ENSO amplitude dependence on strength of nonlinear damping for different linear growth rate regimes. (d) Seasonal ENSO variance (bar graph) and growth rate of ENSO (curves) for observations (OBS) and the RO model. Histogram of (e) El Niño and (f) La Niña peaking month according to calendar months for the observations and the RO model.

fundamental for ENSO phase locking (An & Jin, 2010; Stein et al., 2014).

We use here the simple RO framework to discern the key factors that affect ENSO phase locking, which can be simply measured by the histogram of SSTA variance as a function of calendar month both for the observations and a typical solution from the RO model (Figure 6.10d). Another direct measure for capturing the ENSO peak phase is to examine the histogram of SSTA peak time as a function of calendar month (Figure 6.10e, f). These two methods both capture ENSO phase locking. For the observations, the peak times of both El Niño and La Niña tend to occur toward the end of the calendar year from November to January. The same ENSO phase locking is seen for the RO model simulation. In addition, how narrowly the histogram of SSTA peak time is distributed around the most preferred season is another important characteristic of ENSO phase locking. In both observations and model simulations, the distribution of the peak month is narrower for La Niña than El Niño, indicating that the sharpness of ENSO phase locking is asymmetric. In Chen and Jin (2020), the strength of ENSO phase locking is defined by the sharpness of the ENSO phase histogram. A sharp distribution of the phase histogram indicates a strong phase locking, whereas a wide distribution indicates weak phase locking. Chen and Jin (2020) demonstrated that the preferred month of ENSO peaking time depends on the phase and strength of the seasonal cycle modulation of ENSO growth rate, and the strength of ENSO phase locking mainly depends on the amplitude of the seasonal cycle of the growth rate, the linear growth rate regime, noise, and the linear frequency. Consequently, understanding how the seasonal cycles in the cold tongue and warm pool background states respectively control the phase and strength of seasonal cycle modulation of the ENSO growth rate may help quantify the main contributing sources to ENSO phase locking.

6.4.3. ENSO Periodicity and Frequency Locking

ENSO periodicity appears to span a wide range, from 2 to 7 years in the modern record, with some evidence pointing to the preference of QQ and QB periodicities (Jiang et al., 1995; Ghil et al., 2002). The current generation of climate models still suffers from large biases in the simulation of ENSO periodicity (Lu et al., 2018). What controls ENSO periodicity is a fundamental question and important for understanding its basic dynamics. Linear instability theory, as briefly reviewed in section 6.2, suggests that the linear frequency of the leading ENSO mode varies sensitively from QQ to QB periodicity ranges, with modest changes from a relatively weaker to a stronger cold-tongue basic state. Moreover, the linear eigen frequency is not the sole factor that controls ENSO periodicity. Frequency locking induced by the seasonal cycle (Jin et al., 1994; Tziperman et al., 1994) and nonlinear corrections to ENSO periodicity (demonstrated analytically in the appendix of Jin, 1997a, and numerically in Eccles and Tziperman, 2004) can also affect the ENSO periodicity.

We first examine the frequency-locking phenomenon using the symmetric version of the RO model ($b = B = 0$) in the supercritical regime ($R - \varepsilon > 0$) without noise forcing. We vary the key parameters that control the linear period of RO ENSO $\left(2\pi / \sqrt{\omega_0^2 - \left(\frac{R+\varepsilon}{2} \right)^2} \right)$ and the strength of the annual modulation of the ENSO growth rate (R_a). The dominant frequency (main peak of the SSTA spectrum) is shown in Figure 6.11. The ENSO frequency is discretized into frequency-locked steps known as a Devil's staircase (Bak, 1986), as noted in Jin et al. (1994), and frequency-locked regions that are called Arnold tongues (Arnol'd, 1961), as noted in Jin et al. (1996) and Neelin et al. (1998) in two-parameter space. The dominant ENSO periodicity remains constant over an interval and then changes in discrete jumps to the next frequency-locked solution (e.g., 2, 3, 4, 5, 6, 7, and 8-year periodicities and a series of rational fraction frequencies corresponding to non-integer-year periodicity). When R_a is increased, the width of each frequency step is increased, which indicates stronger frequency locking. ENSO linear instability and the strong seasonal modulation of this linear growth rate tend to generate a preference for QQ or QB ENSO periodicities if the linear ENSO frequency is within the QQ or QB range.

The linear ENSO frequency, as captured by the imaginary part of the BWJ index, is the main factor that controls ENSO periodicity. Seasonal modulations of ENSO, nonlinear processes, and symmetry breaking only have moderate effects on ENSO periodicity. Noise forcing not only can completely smooth out the the 4-, 3- and 2-year periodicity from nonlinear frequency locking but also shift ENSO's main periodicity toward high frequencies due to nonlinear effects (Figure 6.11b). It is difficult to explain the observed broad range of ENSO periodicity with a single linear frequency in the RO model framework. The observed broad spectrum of ENSO likely involves sensitive modulation of ENSO linear periodicity by slow variations in the basic state; however, additional studies are needed to substantiate this conjecture.

6.4.4. ENSO Asymmetry

The causes of the asymmetry between El Niño and La Niña in amplitude, duration, and spatial SST patterns are key questions in ENSO research. While the RO

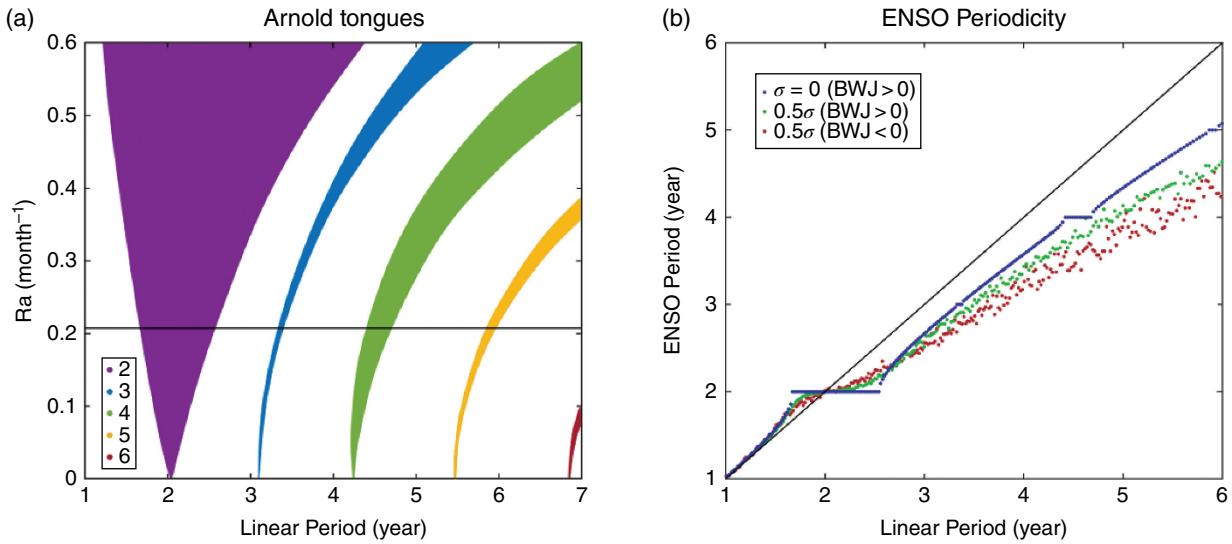

Figure 6.11 (a) Schematic representation of an Arnold tongue diagram for the model. The horizontal black line is related to the Devil's staircase. (b) The Devil's staircase, namely, a plot of the ENSO periodicity as a function of the linear period for different stochastic forcing in the unstable regime (blue and green dots) and stable regime (red dots). The dominant ENSO period is estimated from the maximum peak of the ensemble average of 100-member power spectral density calculated via Fast Fourier Transform (FFT). Each ensemble member is integrated for 200 years.

framework is not able to address the pattern asymmetry, the other asymmetries can be addressed qualitatively with the RO model (Levine & Jin, 2010), as shown in Figure 6.12a–c. A number of processes have been identified to explain ENSO amplitude asymmetry (Jin et al., 2003; An & Jin, 2004; Hayashi & Jin, 2017; Su et al., 2010; Vialard et al., 2001; Kang & Kug, 2002; Liang et al., 2017), and we refer the reader to chapter 7 for a detailed review. Here, we summarize all the processes that generate amplitude asymmetry into two types of symmetry-breaking processes: (i) nonlinear dynamical heating and (ii) ENSO state-dependent deterministic coupled feedback, such as a threshold nonlinearity (Choi et al., 2013; Takahashi et al., 2019) or ENSO state-dependent stochastic excitation. In our RO model framework, without loss of generality, they are related to the parameters b and B, respectively.

The SSTA skewness has been the main measure for ENSO asymmetry. Using the statistical moment approach of Jin et al. (2007) and Levine and Jin (2010), we may obtain the approximated solution for the third moment (skewness) as a nearly linear function of the ENSO symmetry breaking processes, as measured by parameters b and B (not shown). Both the deterministic and stochastic symmetry-breaking processes can generate ENSO asymmetry (Figure 6.12d). Positive ENSO NDH and NDH from TIW can both increase the b parameter that in turn increases positive ENSO skewness. The activity of WWB/MJO and TIW modulated by ENSO will increase the B parameter, and thus also ENSO skewness. If b becomes negative, the effect on skewness also becomes negative. If La Niña can generate more easterly wind bursts, which may not be the case in nature (Hayashi & Watanabe, 2016; Puy et al., 2015), we will then find a linear relation between negative B and ENSO skewness as well. The ENSO linear growth rate regime can also affect ENSO skewness: ENSO skewness decreases when the linear growth rate changes from a stable to an unstable regime. Nevertheless, the key insight learned from the RO model is that the ENSO symmetry breaking processes may all additively contribute to ENSO asymmetry as measured by its SSTA skewness.

6.4.5. Rectification of ENSO onto the Climatological Mean State

As synoptic weather systems transport heat, moisture, and momentum that affect the background mean state in which the weather systems develop, there is also a similar ENSO–mean state interaction through various nonlinear processes. Simple nonlinear conceptual models with nonlinear advection (Jin, 1996; Sun, 1997; Jin, 1998; Timmermann & Jin, 2002; Timmermann et al., 2003; Liang et al., 2012), more complex models (Rodgers et al., 2004), and NDH diagnosed from reanalysis data (Jin et al., 2003; An & Jin, 2004; Hayashi & Jin, 2017) all point toward the importance of ENSO's nonlinear rectification effect on the mean state.

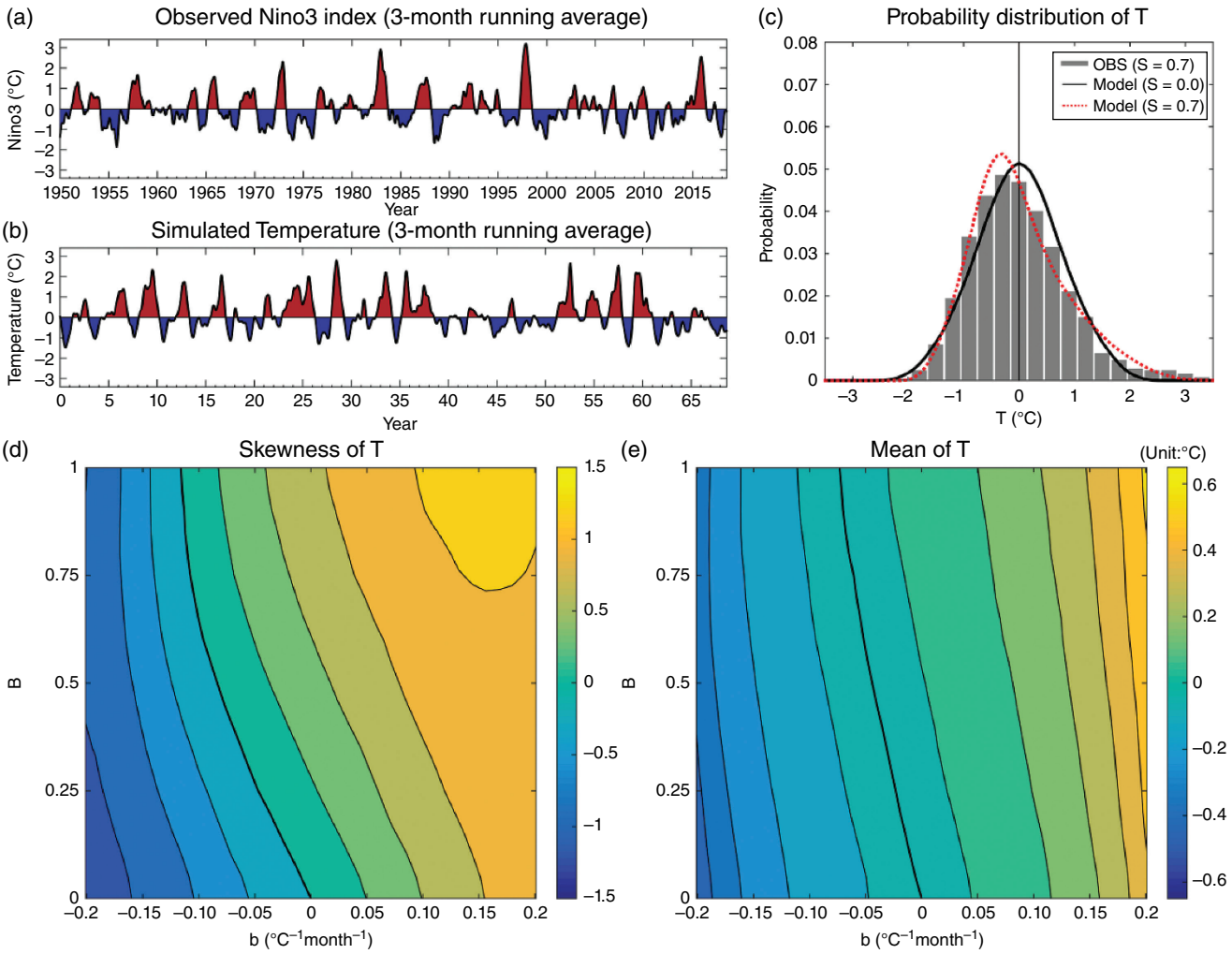

Figure 6.12 (a) Observed Niño-3 index and (b) time series of the model simulated temperature using a three-month running average. (c) Probability distribution of temperature for the observations (gray bar) and RO model with zero (black curve) and normal (red curve) SST skewness values. (d) Skewness of simulated temperature related as a function of state-dependent noise forcing amplitude and quadratic nonlinearity. (e) Mean of simulated temperature as a function of state-dependent noise forcing amplitude and quadratic nonlinearity.

Whether it be the baroclinic instability for weather systems or the Bjerknes instability for ENSO, linear growth can only cause perturbations to grow within a finite timeframe as nonlinearities in the conservation laws of the governing equations (primarily through advective heat redistribution) will generate changes in the mean state to prevent unstable linear growth. A detailed discussion of the specific processes that are important for ENSO–mean state interaction can be found in chapter 8. We here will use the simple RO model to gain insight into the relationship between ENSO's rectification effect onto the mean background state and ENSO skewness through symmetry-breaking nonlinearities.

The time-mean of the SSTA in the RO model can be written as

$$\left(R-\frac{\omega_0^2}{\varepsilon}\right)\overline{T_E}+b\overline{T_E^2}-c\overline{T_E^3}+\sigma B\overline{\xi T_E}=0. \qquad (6.39)$$

In the absence of symmetry-breaking processes ($b = B = 0$), the time-mean solution is zero and there is no mean state change even though the system is nonlinear. This is because the cubic nonlinearity in SST and the additive noise are symmetry-preserving nonlinearities. However, once the symmetry is broken by either state-dependent noise or a quadratic nonlinearity, both of which can be easily related to ubiquitous advective processes, all the

nonlinear terms give rise to nonzero contributions to a time-mean NDH. Considering the fact that the time-mean SSTAs are small, the time mean of nonlinear terms and multiplicative noise terms in Eq. (6.39) are dominated by $b\overline{T_E{}'^2} - c\overline{T_E{}'^3} + \sigma B\overline{\xi T_E{}'}$. Furthermore, we can obtain a linear analytical solution to demonstrate that a positive ENSO-like warming mean state is proportional to the skewness of ENSO $\overline{T_E} \propto S$, as demonstrated in Figure 6.12d and 12e. The time-mean temperature is linearly related to the ENSO skewness. This simple relation provides a tool for us to understand how ENSO may not only affect but also interact with the cold tongue mean state in the tropical Pacific and how biases in climate model simulations of ENSO may contribute to a climate mean state bias.

6.5. OUTLOOK

Modern observational networks, deployed just in the past few decades, have already captured a rich variety of ENSO spatial patterns and temporal evolutions, as described in chapters 3 and 4, among others. These short records have most likely not yet encapsulated the full spectrum of possible ENSO behaviors. Nevertheless, the complexity we have seen has gone far beyond what was perceived by pioneers such as Bjerknes and Wyrtki, among others. Significant advances have indeed been made in the theory of ENSO complexity (e.g., JN93; Neelin et al., 1998; Fedorov & Philander, 2001; Jin et al., 2006; Levine & Jin, 2010; Stuecker et al., 2013; Takahashi et al., 2019; Xie & Jin, 2018), in comprehensive simulations of ENSO by climate models (e.g., Guilyardi et al., 2009; Wittenberg et al., 2014; Bayr et al., 2018), and in improving operational predictions of ENSO events and their climatic and societal impacts (e.g., Luo et al., 2008; McPhaden et al., 2010; Stockdale et al., 2011; Barnston et al., 2012; L'Heureux et al., 2017). In spite of the tremendous successes achieved, state-of-the-art climate models are yet to converge in their simulations of basic ENSO characteristics such as its amplitude, period, phase locking, and warm-cold phase asymmetry. Even more challenging is for models to simulate these characteristics as a result of capturing all key processes in the right balance, instead of as a result of error compensations (Bellenger et al., 2014; Karamperidou et al., 2017; Bayr et al., 2018; chapter 9 in this book). An additional challenge for models is the simulation of ENSO diversity, characterized by distinct spatial patterns, periodicities, duration, and asymmetries of the different ENSO "flavors." These model biases have likely stalled the improvement of the skill and reliability of dynamical seasonal climate predictions that depend heavily on the representation of ENSO in climate models. Identifying the sources and understanding the underlying mechanisms of stubborn climate model biases in the simulation of the mean state of the equatorial Pacific and the representation of ENSO thermodynamic and dynamic feedbacks will be essential in developing the next generation of models for seamless climate forecasts and projections. Future research on ENSO complexity needs to continue to undertake a hierarchical modeling approach that includes simple conceptual models, models of intermediate complexity with consistent thermodynamic and dynamic coupled feedback processes and representation of multiscale interactions, and state-of-the-art high-resolution general circulation models (chapter 9 in this book). This long-tested hierarchical approach that combines theoretical, observational, model, and diagnostic frameworks has the potential to lead to a new era of advances in ENSO research, advances that will not only enhance our understanding of the fundamental dynamics of eastern and central Pacific ENSO events, their interactions, and their relation to tropical Pacific decadal variability, but also decipher the role of multiscale processes involving WWBs, TIWs, and extratropical and pan-basin precursors of ENSO spatiotemporal complexity. These are essential steps to ultimately improve predictive skill for the entire tropical-extratropical climate system.

ACKNOWLEDGMENTS

The authors are grateful for valuable comments from Mark Cane, Alexey Fedorov, and an anonymous reviewer. F.F.J. was supported by US NSF grant AGS-1813611 and Department of Energy grant DE-SC0005110. M.H. was supported by JSPS Overseas Research Fellowships 201860671. C.K. was supported by US NSF grant #AGS-1602097. M.F.S. was supported by the Institute for Basic Science (project code IBS-R028-D1). R.X. was supported by the National Natural Science Foundation of China (NSFC Grant 41506017).

A BRIEF DESCRIPTION OF THE CZ MODEL

The CZ model is an anomaly model with a prescribed annually varying climate mean state. It comprises a simple quasi-linear Gill-Matsuno atmospheric component (Zebiak & Cane, 1987) that simulates the tropical wind response to ENSO-associated SSTAs by considering condensational heating due to SSTA-induced moisture supply through evaporation and convective heating parameterized by moisture convergence by anomalous atmospheric flow:

$$\varepsilon_a u_a^n - \beta_0 y v_a^n = -\left(p^n / \rho_0\right)_x, \qquad \text{(A1a)}$$

$$\varepsilon_a v_a{}^n + \beta_0 y u_a{}^n = -\left(p^n / \rho_0\right)_y, \tag{A1b}$$

$$\varepsilon_a \left(p^n / \rho_0\right) + c_a{}^2 \left[\left(u_a{}^n\right)_x + \left(v_a{}^n\right)_y\right] = -\dot{Q}_s - \dot{Q}_1{}^{n-1}, \tag{A1c}$$

$$\dot{Q}_s = (\alpha T)\exp\left[\left(\bar{T} - 30\right)/16.7\right], \tag{A1d}$$

$$\dot{Q}_1{}^n = \beta\left[M\left(\bar{c} + c^n\right) - M\left(\bar{c}\right)\right]. \tag{A1e}$$

Definitions for all variables and parameters are listed in Table A. Here n denotes the sequence such that cumulus convection parameterized from moisture convergence can be solved iteratively.

The oceanic dynamical component includes a 1.5-layer linear reduced gravity model that describes the upper-layer current and thermocline depth anomalies in response to wind stress anomalies:

$$\frac{\partial u}{\partial t} - \beta_0 y v = -g' \frac{\partial h}{\partial x} + \frac{\tau^x}{\rho H} - ru \tag{A2a}$$

$$\beta_0 y u = -g' \frac{\partial h}{\partial y} + \frac{\tau^y}{\rho H} - rv \tag{A2b}$$

$$\frac{\partial h}{\partial t} + H\left(\frac{\partial u}{\partial x} + \frac{\partial v}{\partial y}\right) = -rh, \tag{A2c}$$

where $\mathbf{u} = H^{-1}(H_1\mathbf{u}_1 + H_2\mathbf{u}_2)$. The subscripts 1 and 2 indicate that within the upper layer ocean, there is an embedded mixed layer with fixed depth H_1 (50 m) and an underlying subsurface layer with fixed depth H_2 (100 m). The equations governing the velocity shear ($\mathbf{u}_s$) between layer 1 and 2 are

$$r_s u_s - \beta_0 y v_s = \frac{\tau^x}{\rho H_1}, \tag{A3a}$$

$$r_s v_s + \beta_0 y u_s = \frac{\tau^y}{\rho H_1}, \tag{A3b}$$

where $\mathbf{u}_s = \mathbf{u}_1 - \mathbf{u}_2$.

The mixed-layer SSTA is governed by the heat budget

$$\frac{\partial T}{\partial t} = -\mathbf{u}_1 \cdot \nabla\left(\bar{T} + T\right) - \bar{\mathbf{u}}_1 \cdot \nabla T - \left\{M\left(\bar{w}_s + w_s\right) - M\left(\bar{w}_s\right)\right\} \times \bar{T}_z$$

$$-M\left(\bar{w}_s + w_s\right)\frac{T - T_e}{H_1} - \alpha_s T, \tag{A4a}$$

$$T_e = \gamma T_{sub} + (1 - \gamma)T, \tag{A4b}$$

$$T_{sub}(h) = \begin{cases} T_1\left\{\tanh\left[b_1\left(\bar{h} + h\right)\right] - \tanh\left(b_1\bar{h}\right)\right\}, & h > 0 \\ T_2\left\{\tanh\left[b_2\left(\bar{h} - h\right)\right] - \tanh\left(b_2\bar{h}\right)\right\}, & h < 0 \end{cases}, \tag{A4c}$$

where $\bar{T}$, $\bar{\mathbf{u}}_1$, and $\bar{w}_s$ are the mean SST, horizontal mixed-layer ocean currents, and upwelling. Parameters and their values used in the model are listed in Table A.

REFERENCES

An, S.-I. (2008). Interannual variations of the tropical ocean instability wave and ENSO. *Journal of Climate*, *21*(15), 3680–3686. https://doi.org/10.1175/2008JCLI1701.1

An, S.-I., & Jin, F.-F. (2000). An eigen analysis of the interdecadal changes in the structure and frequency of ENSO mode. *Geophysical Research Letters*, *27*(16), 2573–2576. https://doi.org/10.1029/1999GL011090

An, S.-I., & Jin, F.-F. (2004). Nonlinearity and asymmetry of ENSO. *Journal of Climate*, *17*(12), 2399–2412. https://doi.org/10.1175/1520-0442(2004)017%3C2399:NAAOE%3E2.0.CO;2

An, S.-I., & Jin, F.-F. (2010). Linear solutions for the frequency and amplitude modulation of ENSO by the annual cycle. *Tellus A*, *63*(2), 238–243. https://doi.org/10.1111/j.1600-0870.2010.00482.x

Arnol'd, V. I. (1961). Small denominators: I. Mapping the circle onto itself. *Izvestiya Rossiiskoi Akademii Nauk SSSR Seriya Matematicheskaya*, *25*(1), 21–86.

Bak, P. (1986). Devil's staircase. *Physics Today*, *39*(12), 38. https://doi.org/10.1063/1.881047

Barnston, A. G., Tippett, M. K., L'Heureux, M. L., Li, S., & DeWitt, D. G. (2012). Skill of real-time seasonal ENSO model predictions during 2002–11: Is our capability increasing? *Bulletin of the American Meteorological Society*, *93*(5), 631–651. https://doi.org/10.1175/BAMS-D-11-00111.1

Battisti, D. S., & Hirst, A. C. (1989). Interannual variability in a tropical atmosphere-ocean model: Influence of the basic state, ocean geometry and nonlinearity. *Journal of the Atmospheric Sciences*, *46*(12), 1687–1712. https://doi.org/10.1175/1520-0469(1989)046%3C1687:IVIATA%3E2.0.CO;2

Bayr, T., Latif, M., Dommenget, D., Wengel, C., Harlaß, J., & Park, W. (2018). Mean-state dependence of ENSO atmospheric feedbacks in climate models. *Climate Dynamics*, *50*(9–10), 3171–3194. https://doi.org/10.1007/s00382-017-3799-2

Bejarano, L. (2006). *Coexistence of leading equatorial coupled modes for ENSO* (Ph.D. dissertation). Retrieved from FSU Digital Library (http://purl.flvc.org/fsu/fd/FSU_migr_etd-1210). Tallahassee, FL: Florida State University.

Bejarano, L., & Jin, F.-F. (2008). Coexistence of equatorial coupled modes of ENSO. *Journal of Climate*, *21*(12), 3051–3067. https://doi.org/10.1175/2007JCLI1679.1

Bellenger, H., Guilyardi, E., Leloup, J., Lengaigne, M., & Vialard, J. (2014). ENSO representation in climate models: From CMIP3 to CMIP5. *Climate Dynamics*, *42*(7–8), 1999–2018. https://doi.org/10.1007/s00382-013-1783-z

Bjerknes, J. (1969). Atmospheric teleconnections from the equatorial Pacific. *Monthly Weather Review*, *97*(3), 163–172. https://doi.org/10.1175/1520-0493(1969)097%3C0163:ATFTEP%3E2.3.CO;2

Bjerknes, J., & Solberg, H. (1922). Life cycle of cyclones and the polar front theory of atmospheric circulation. *Geofysiske Publikationer*, *3*(1), 3–18.

Boucharel, J., & Jin, F.-F. (2020). A simple theory for the modulation of tropical instability waves by ENSO and the annual cycle. *Tellus A*, *72*(1), 1–14. https://doi.org/10.1080/16000870.2019.1700087

Burgers, G., Jin, F.-F., & van Oldenborgh, G. J. (2005). The simplest ENSO recharge oscillator. *Geophysical Research Letters*, *32*, L13706. https://doi.org/10.1029/2005GL022951

Cane, M. A. (1984). Modeling sea level during El Niño. *Journal of Physical Oceanography*, *14*, 1864–1874. https://doi.org/10.1175/1520-0485(1984)014%3C1864:MSLDEN%3E2.0.CO;2

Cane, M. A., Münnich, M., & Zebiak, S. E. (1990). A study of self-excited oscillations of the tropical ocean-atmosphere system: I. Linear analysis. *Journal of the Atmospheric Sciences*, *47*, 1562–1577. https://doi.org/10.1175/1520-0469(1990)047%3C1562:ASOSEO%3E2.0.CO;2

Cane, M. A., & Sarachik, E. S. (1977). Forced baroclinic ocean motions: II. The linear equatorial bounded case. *Journal of Marine Research*, *35*, 395–432.

Cane, M. A., & Sarachik, E. S. (1979). Forced baroclinic ocean motions: III. The linear equatorial basin case. *Journal of Marine Research*, *37*, 355–398.

Cane, M. A., & Sarachik, E. S. (1981). The response of a linear baroclinic equatorial ocean to periodic forcing. *Journal of Marine Research*, *39*(4), 651–693.

Cane, M. A., & Zebiak, S. E. (1985). A theory for El Niño and the Southern Oscillation. *Science*, *228*(4703), 1085–1087. https://doi.org/10.1126/science.228.4703.1085

Cane, M. A., Zebiak, S. E., & Dolan, S. C. (1986). Experimental forecasts of El Niño. *Nature*, *321*(6073), 827. https://doi.org/10.1038/321827a0

Carton, J. A., Chepurin, G. A., & Chen, L. (2018). SODA3: A new ocean climate reanalysis. *Journal of Climate*, *31*(17), 6967–6983. https://doi.org/10.1175/JCLI-D-18-0149.1

Chen, H.-C. & Jin, F.-F. (2020). Fundamental behavior of ENSO phase-locking. *Journal of Climate*, *33*(5), 1953–1968. https://doi.org/10.1175/JCLI-D-19-0264.1

Chen, N., & Majda, A. J. (2016). Simple dynamical models capturing the key features of the central Pacific El Niño. *Proceedings of the National Academy of Sciences*, *113*(42), 11732–11737. https://doi.org/10.1073/pnas.1614533113

Chen, N., & Majda, A. J. (2017). Simple stochastic dynamical models capturing the statistical diversity of El Niño Southern Oscillation. *Proceedings of the National Academy of Sciences*, *114*(7), 1468–1473. https://doi.org/10.1073/pnas.1620766114

Choi, K.-Y., Vecchi, G. A., & Wittenberg, A. T. (2013). ENSO transition, duration, and amplitude asymmetries: Role of the nonlinear wind stress coupling in a conceptual model. *Journal of Climate*, *26*(23), 9462–9476. https://doi.org/10.1175/JCLI-D-13-00045.1

Dijkstra, H. A. (2005). *Nonlinear physical oceanography: A dynamical systems approach to the large scale ocean circulation and El Niño*. Dordrecht, NY: Springer.

Eccles, F., & Tziperman, E. (2004). Nonlinear effects on ENSO's period. *Journal of the Atmospheric Sciences*, *61*(4), 474–482. https://doi.org/10.1175/1520-0469(2004)061%3C0474:NEOEP%3E2.0.CO;2

Eisenman, I., Yu, L., & Tziperman, E. (2005). Westerly wind bursts: ENSO's tail rather than the dog? *Journal of Climate*, *18*(24), 5224–5238. https://doi.org/10.1175/JCLI3588.1

Fedorov, A. V. (2010). Ocean response to wind variations, warm water volume, and simple models of ENSO in the low-frequency approximation. *Journal of Climate*, *23*, 3855–3873. https://doi.org/10.1175/2010JCLI3044.1

Fedorov, A. V., & Philander, S. G. (2000). Is El Niño changing? *Science*, *288*(5473), 1997–2002. https://doi.org/10.1126/science.288.5473.1997

Fedorov, A. V., & Philander, S. G. (2001). A stability analysis of tropical ocean-atmosphere interactions: Bridging measurements and theory for El Niño. *Journal of Climate*, *14*(14), 3086–3101. https://doi.org/10.1175/1520-0442(2001)014%3C3086:ASAOTO%3E2.0.CO;2

Fedorov, A. V., Harper, S. L., Winter, B. & Wittenberg, A. (2003). How predictable is El Niño? *Bulletin of the American Meteorological Society*, *84*(7), 911–919. https://doi.org/10.1175/BAMS-84-7-911

Ghil, M., Allen, M. R., Dettinger, M. D., Ide, K., Kondrashov, D., Mann, M. E., et al. (2002). Advanced spectral methods for climatic time series. *Reviews of Geophysics*, *40*(1), 1003. https://doi.org/10.1029/2000RG000092

Gill, A. E. (1980). Some simple solutions for heat-induced tropical circulation. *Quarterly Journal of the Royal Meteorological Society*, *106*(449), 447–462. https://doi.org/10.1002/qj.49710644905

Gill, A. E. (1985). Elements of coupled ocean-atmosphere models for the tropics. In J.C.J. Nihoul (Ed.), *Coupled ocean-atmosphere models* (Elsevier Oceanography Series, Vol. *40*, pp. 303–327). Liège, Belgium: Elsevier. https://doi.org/10.1016/S0422-9894(08)70718-9

Guilyardi, E., Wittenberg, A., Fedorov, A., Collins, M., Wang, C., Capotondi, A., et al. (2009). Understanding El Niño in ocean-atmosphere general circulation models: Progress and challenges. *Bulletin of the American Meteorological Society*, *90*(3), 325–340. https://doi.org/10.1175/2008BAMS2387.1

Hayashi, M., & Jin, F.-F. (2017). Subsurface nonlinear dynamical heating and ENSO asymmetry. *Geophysical Research Letters*, *44*(24), 12427–12435. https://doi.org/10.1002/2017GL075771

Hayashi, M., & Watanabe, M. (2016). Asymmetry of westerly and easterly wind events: Observational evidence. *Scientific Online Letters on the Atmosphere*, *12*, 38–41. https://doi.org/10.2151/sola.2016-009

Hirst, A. C. (1986). Unstable and damped equatorial modes in simple coupled ocean-atmosphere models. *Journal of the*

Atmospheric Sciences, *43*(6), 606–632. https://doi.org/10.1175/1520-0469(1986)043%3C0606:UADEMI%3E2.0.CO;2

Izumo, T., Lengaigne, M., Vialard, J., Suresh, I., & Planton, Y. (2019). On the physical interpretation of the lead relation between warm water volume and the El Niño Southern Oscillation. *Climate Dynamics*, *52*(5–6), 2923–2942. https://doi.org/10.1007/s00382-018-4313-1

Jiang, N., Neelin, J. D., & Ghil, M. (1995). Quasi-quadrennial and quasi-biennial variability in the equatorial Pacific. *Climate Dynamics*, *12*(2), 101–112. https://doi.org/10.1007/BF00223723

Jin, F.-F. (1996). Tropical ocean-atmosphere interaction, the Pacific cold tongue, and the El Niño-Southern Oscillation. *Science*, *274*(5284), 76–78. https://doi.org/10.1126/science.274.5284.76

Jin, F.-F. (1997a). An equatorial ocean recharge paradigm for ENSO: Part I. Conceptual model. *Journal of the Atmospheric Sciences*, *54*(7), 811–829. https://doi.org/10.1175/1520-0469(1997)054%3C0811:AEORPF%3E2.0.CO;2

Jin, F.-F. (1997b). An equatorial recharge paradigm for ENSO: II. A stripped-down coupled model. *Journal of the Atmospheric Sciences*, *54*(7), 830–847. https://doi.org/10.1175/1520-0469(1997)054%3C0830:AEORPF%3E2.0.CO;2

Jin, F.-F. (1998). A simple model for the Pacific cold tongue and ENSO. *Journal of the Atmospheric Sciences*, *55*(14), 2458–2469. https://doi.org/10.1175/1520-0469(1998)055%3C2458:ASMFTP%3E2.0.CO;2

Jin, F.-F., & An, S.-I. (1999). Thermocline and zonal advective feedbacks within the equatorial ocean recharge oscillator model for ENSO. *Geophysical Research Letters*, *26*(19), 2989–2992. https://doi.org/10.1029/1999GL002297

Jin, F.-F., & Neelin, J. D. (1993a). Modes of interannual tropical ocean-atmosphere interaction—A unified view. Part I: Numerical results. *Journal of the Atmospheric Sciences*, *50*(21), 3477–3503. https://doi.org/10.1175/1520-0469(1993)050%3C3477:MOITOI%3E2.0.CO;2

Jin, F.-F., & Neelin, J. D. (1993b). Modes of interannual tropical ocean-atmosphere interaction—A unified view. Part III: Analytical results in fully coupled cases. *Journal of the Atmospheric Sciences*, *50*(21), 3523–3540. https://doi.org/10.1175/1520-0469(1993)050%3C3523:MOITOI%3E2.0.CO;2

Jin, F.-F., Neelin, J. D., & Ghil, M. (1994). El Niño on the Devil's staircase: Annual subharmonic steps to chaos. *Science*, *264*(5155), 70–72. https://doi.org/10.1126/science.264.5155.70

Jin, F.-F., Neelin, J. D., & Ghil, M. (1996). El Niño/Southern Oscillation and the annual cycle: Subharmonic frequency-locking and aperiodicity. *Physica D: Nonlinear Phenomena*, *98*(2–4), 442–465. https://doi.org/10.1016/0167-2789(96)00111-X

Jin, F.-F., An, S.-I., Timmermann, A., & Zhao, J. (2003). Strong El Niño events and nonlinear dynamical heating. *Geophysical Research Letters*, *30*(3), 1120. https://doi.org/10.1029/2002GL016356

Jin, F.-F., Kim, S. T., & Bejarano, L. (2006). A coupled-stability index for ENSO. *Geophysical Research Letters*, *33*(23), L23708. https://doi.org/10.1029/2006GL027221

Jin, F.-F., Lin, L., Timmermann, A., & Zhao, J. (2007). Ensemble-mean dynamics of the ENSO recharge oscillator under state-dependent stochastic forcing. *Geophysical Research Letters*, *34*(3), L03807. https://doi.org/10.1029/2006GL027372

Kang, I.-S., & Kug, J.-S. (2002). El Niño and La Niña sea surface temperature anomalies: Asymmetry characteristics associated with their wind stress anomalies. *Journal of Geophysical Research*, *107*(D19), 4372. https://doi.org/10.1029/2001JD000393

Karamperidou, C., Jin, F.-F. & Conroy, J. L. (2017). The importance of ENSO nonlinearities in tropical Pacific response to external forcing. *Climate Dynamics*, *49*(7–8), 2695–2704. https://doi.org/10.1007/s00382-016-3475-y

Kessler, W. S. (2002). Is ENSO a cycle or a series of events? *Geophysical Research Letters*, *29*(23), 2125. https://doi.org/10.1029/2002GL015924

Kessler, W. S., McPhaden, M. J., & Weickmann, K. M. (1995). Forcing of intraseasonal Kelvin waves in the equatorial Pacific. *Journal of Geophysical Research*, *100*(C6), 10613–10631. https://doi.org/10.1029/95JC00382

Kim, S. T., Cai, W., Jin, F.-F., & Yu, J.-Y. (2014). ENSO stability in coupled climate models and its association with mean state. *Climate Dynamics*, *42*(11–12), 3313–3321. https://doi.org/10.1007/s00382-013-1833-6

Kim, S. T., & Jin, F.-F. (2011). An ENSO stability analysis. Part I: Results from a hybridcoupled model. *Climate Dynamics*, *36*(7–8), 1593–1607. https://doi.org/10.1007/s00382-010-0796-0

Kleeman, R., & Moore, A. M. (1997). A theory for the limitation of ENSO predictability due to stochastic atmospheric transients. *Journal of the Atmospheric Sciences*, *54*(6), 753–767. https://doi.org/10.1175/1520-0469(1997)054<0753:ATFTLO>2.0.CO;2

Kug, J.-S., Jin, F.-F., & An, S.-I. (2009). Two types of El Niño events: Cold tongue El Niño and warm pool El Niño. *Journal of Climate*, *22*(6), 1499–1515. https://doi.org/10.1175/2008JCLI2624.1

Launder, B. E., Reece, G. J., & Rodi, W. (1975). Progress in the development of a Reynolds-stress turbulence closure. *Journal of Fluid Mechanics*, *68*(3), 537–566. https://doi.org/10.1017/S0022112075001814

Lengaigne, M., Guilyardi, E., Boulanger, J. P., Menkes, C., Delecluse, P., Inness, P., Cole, J., & Slingo, J. (2004). Triggering of El Niño by westerly wind events in a coupled general circulation model. *Climate Dynamics*, *23*(6), 601–620. https://doi.org/10.1007/s00382-004-0457-2

Levine, A. F. Z., & Jin, F.-F. (2010). Noise-induced instability in the ENSO recharge oscillator. *Journal of the Atmospheric Sciences*, *67*(2), 529–542. https://doi.org/10.1175/2009JAS3213.1

Levine, A. F. Z., & McPhaden, M. J. (2016). How the July 2014 easterly wind burst gave the 2015–2016 El Niño a head start. *Geophysical Research Letters*, *43*(12), 6503–6510. https://doi.org/10.1002/2016GL069204

L'Heureux, M. L., Takahashi, K., Watkins, A. B., Barnston, A. G., Becker, E. J., Di LiBerto, T. E., et al. (2017). Observing and predicting the 2015/16 El Niño. *Bulletin of the American Meteorological Society*, *97*(7), 1363–1382. https://doi.org/10.1175/BAMS-D-16-0009.1

Liang, J., Yang, X.-Q., & Sun, D.-Z. (2012). The effect of ENSO events on the tropical Pacific mean climate: Insights from an analytical model. *Journal of Climate*, *25*(21), 7590–7606. https://doi.org/10.1175/JCLI-D-11-00490.1

Liang, J., Yang, X.-Q., & Sun, D.-Z. (2017). Factors determining the asymmetry of ENSO. *Journal of Climate*, *30*(16), 6097–6106. https://doi.org/10.1175/JCLI-D-16-0923.1

Lindzen, R. S., & Nigam, S. (1987). On the role of sea surface temperature gradients in forcing low-level winds and convergence in the tropics. *Journal of the Atmospheric Sciences*, *44*(17), 2418–2436. https://doi.org/10.1175/1520-0469(1987)044%3C2418:OTROSS%3E2.0.CO;2

Lu, B., Jin, F.-F., & Ren, H.-L. (2018). A coupled dynamic index for ENSO periodicity. *Journal of Climate*, *31*(6), 2361–2376. https://doi.org/10.1175/JCLI-D-17-0466.1

Luo, J.-J., Masson, S., Behera, S. K., & Yamagata, T. (2008). Extended ENSO predictions using a fully coupled ocean-atmosphere model. *Journal of Climate*, *21*(1), 84–93. https://doi.org/10.1175/2007JCLI1412.1

Matsuno, T. (1966). Quasi-geostrophic motions in the equatorial area. *Journal of the Meteorological Society of Japan*. *Ser. II*, *44*(1), 25–43. https://doi.org/10.2151/jmsj1965.44.1_25

McGregor, S., Timmermann, A., Schneider, N., Stuecker, M. F., & England, M. H. (2012). The effect of the South Pacific convergence zone on the termination of El Niño events and the meridional asymmetry of ENSO. *Journal of Climate*, *25*(16), 5566–5586. https://doi.org/10.1175/JCLI-D-11-00332.1

McPhaden, M. J. (2004). Evolution of the 2002/03 El Niño. *Bulletin of the American Meteorological Society*, *85*(5), 677–695. https://doi.org/10.1175/BAMS-85-5-677

McPhaden, M. J., Busalacchi, A. J., & Anderson, D. L. T. (2010). A TOGA retrospective. *Oceanography*, *23*(3), 86–103. https://doi.org/10.5670/oceanog.2010.26

Moore, D. W. (1968). *Planetary-gravity waves in an equatorial ocean* (Ph.D. Dissertation). Retrieved from Harvard College Library. Cambridge, MA: Harvard University.

Neelin, J. D. (1990). A hybrid coupled general circulation model for El Niño studies. *Journal of the Atmospheric Sciences*, *47*(5), 674–693. https://doi.org/10.1175/1520-0469(1990)047%3C0674:AHCGCM%3E2.0.CO;2

Neelin, J. D., & Jin, F.-F. (1993). Modes of interannual tropical ocean-atmosphere interaction—A unified view. Part II: Analytical results in the weak-coupling limit. *Journal of the Atmospheric Sciences*, *50*(21), 3504–3522. https://doi.org/10.1175/1520-0469(1993)050%3C3504:MOITOI%3E2.0.CO;2

Neelin, J. D., Latif, M., & Jin, F.-F. (1994). Dynamics of coupled ocean-atmosphere models: The tropical problem. *Annual Review of Fluid Mechanics*, *26*, 617–659. https://doi.org/10.1146/annurev.fl.26.010194.003153

Neelin, J. D., Battisti, D., Hirst, A., Jin, F.-F., Wakata, Y., Yamagata, T., & Zebiak, S. E. (1998). ENSO theory. *Journal of Geophysical Research*, *103*(C7), 14262–14290. https://doi.org/10.1029/97JC03424

Neelin, J. D., Jin, F.-F., & Syu, H.-H. (2000). Variations in ENSO phase locking. *Journal of Climate*, *13*(14), 2570–2590. https://doi.org/10.1175/1520-0442(2000)013%3C2570:VIEPL%3E2.0.CO;2

Neske, S., & McGregor, S. (2018). Understanding the warm water volume precursor of ENSO events and its interdecadal variation. *Geophysical Research Letters*, *45*(3), 1577–1585. https://doi.org/10.1002/2017GL076439

Philander, S. G. (Ed.). (1990). *El Niño, La Niña, and the Southern Oscillation*. London, UK: Academic Press.

Philander, S. G., & Fedorov, A. (2003). Is El Niño sporadic or cyclic? *Annual Review of Earth and Planetary Sciences*, *31*, 579–594. https://doi.org/10.1146/annurev.earth.31.100901.141255

Philander, S. G. H., Yamagata, T., & Pacanowski, R. C. (1984). Unstable air-sea interactions in the tropics. *Journal of the Atmospheric Sciences*, *41*(4), 604–613. https://doi.org/10.1175/1520-0469(1984)041<0604:UASIIT>2.0.CO;2

Picaut, J., Masia, F., & du Penhoat, Y. (1997). An advective-reflective conceptual model for the oscillatory nature of the ENSO. *Science*, *277*(5326), 633–666. https://doi.org/10.1126/science.277.5326.663

Planton, Y., Vialard, J., Guilyardi, E., Lengaigne, M., & Izumo, T. (2018). Western Pacific oceanic heat content: A better predictor of La Niña than of El Niño. *Geophysical Research Letters*, *45*(18), 9824–9833. https://doi.org/10.1029/2018GL079341

Puy, M., Vialard, J., Lengaigne, M., & Guilyardi, E. (2015). Modulation of equatorial Pacific westerly/easterly wind events by the Madden-Julian oscillation and convectively-coupled Rossby waves. *Climate Dynamics*, *46*(7–8), 2155–2178. https://doi.org/10.1007/s00382-015-2695-x

Ren, H.-L., & Jin, F.-F. (2013). Recharge oscillator mechanisms in two types of ENSO. *Journal of Climate*, *26*(17), 6506–6523. https://doi.org/10.1175/JCLI-D-12-00601.1

Rodgers, K. B., Friederichs, P., & Latif, M. (2004). Tropical Pacific decadal variability and its relation to decadal modulations of ENSO. *Journal of Climate*, *17*(19), 3761–3774. https://doi.org/10.1175/1520-0442(2004)017%3C3761:TPDVAI%3E2.0.CO;2

Stein, K., Timmermann, A., Schneider, N., Jin, F.-F., & Stuecker, M. F. (2014). ENSO seasonal synchronization theory. *Journal of Climate*, *27*(14), 5285–5310. https://doi.org/10.1175/JCLI-D-13-00525.1

Stockdale, T.N., Anderson, D.L.T., Balmaseda, M.A., Doblas-Reyes, F., Ferranti, L., Mogensen, K., et al. (2011). ECMWF seasonal forecast system 3 and its prediction of sea surface temperature. *Climate Dynamics*, *37*(3–4), 455–471. https://doi.org/10.1007/s00382-010-0947-3

Stuecker, M. F., Timmermann, A., Jin, F.-F., McGregor, S., & Ren, H.-L. (2013). A combination mode of the annual cycle and the El Niño/Southern Oscillation. *Nature Geoscience*, *6*(7), 540–544. https://doi.org/10.1038/ngeo1826

Stuecker, M. F., Jin, F.-F., & Timmermann, A. (2015a). El Niño-Southern Oscillation frequency cascade. *Proceedings of the National Academy of Sciences*, *112*(44), 13490–13495. https://doi.org/10.1073/pnas.1508622112

Stuecker, M. F., Jin, F.-F., Timmermann, A., & McGregor, S. (2015b). Combination mode dynamics of the anomalous northwest Pacific anticyclone. *Journal of Climate*, *28*(3), 1093–1111. https://doi.org/10.1175/jcli-d-14-00225.1

Su, J., Zhang, R., Li, T., Rong, X., Kug, J.-S., & Hong, C.-C. (2010). Causes of the El Niño and La Niña amplitude asymmetry in the equatorial eastern Pacific. *Journal of Climate*, *23*(3), 605–617. https://doi.org/10.1175/2009JCLI2894.1

Suarez, M. J., & Schopf, P. S. (1988). A delayed action oscillator for ENSO. *Journal of the Atmospheric Sciences*, *45*(21), 3283–3287. https://doi.org/10.1175/1520-0469(1988)045%3C3283:ADAOFE%3E2.0.CO;2

Sun, D.-Z. (1997). El Niño: A coupled response to radiative heating? *Geophysical Research Letters*, *24*(16), 2031–2034. https://doi.org/10.1029/97GL01960

Takahashi, K., Karamperidou, C., & Dewitte, B. (2019). A theoretical model of strong and moderate El Niño regimes. *Climate Dynamics*, *52*(12), 7477–7493. https://doi.org/10.1007/s00382-018-4100-z

Timmermann, A., & Jin, F.-F. (2002). A nonlinear mechanism for decadal El Niño amplitude changes. *Geophysical Research Letters*, *29*(1), 1003. https://doi.org/10.1029/2001GL013369

Timmermann, A., Jin, F.-F., & Abshagen, J. (2003). A nonlinear theory for El Niño bursting. *Journal of the Atmospheric Sciences*, *60*(1), 152–165. https://doi.org/ 10.1175/1520-0469(2003)060<0152:ANTFEN>2.0.CO;2

Timmermann, A., An, S.-I., Kug, J.-S., Jin, F.-F., Cai, W., Capotondi, et al. (2018). El Niño-Southern Oscillation complexity. *Nature*, *559*(7715), 535–545. https://doi.org/10.1038/s41586-018-0252-6

Tziperman, E., Stone, L., Cane, M. A., & Jarosh, H. (1994). El Niño chaos: Overlapping of resonances between the seasonal cycle and the Pacific ocean-atmosphere oscillator. *Science*, *264*(5155), 72–74. https://doi.org/10.1126/science.264.5155.72

Tziperman, E., Zebiak, S. E., & Cane, M. A. (1997). Mechanisms of seasonal-ENSO interaction. *Journal of the Atmospheric Sciences*, *54*(1), 61–71. https://doi.org/10.1175/1520-0469(1997)054%3C0061:MOSEI%3E2.0.CO;2

Tziperman, E., Cane, M. A., Zebiak, S. E., Xue, Y., & Blumenthal, B. (1998). Locking of El Niño's peak time to the end of the calendar year in the delayed oscillator picture of ENSO. *Journal of Climate*, *11*(9), 2191–2199. https://doi.org/10.1175/1520-0442(1998)011<2191:LOENOS>2.0.CO;2

Vecchi, G. A., & Harrison, D. E. (2000). Tropical Pacific sea surface temperature anomalies, El Niño and equatorial westerly events. *Journal of Climate*, *13*(11), 1814–1830. https://doi.org/10.1175/1520-0442(2000)013<1814:TPSSTA>2.0.CO;2

Vecchi, G. A., & Harrison, D. E. (2006). The termination of the 1997–98 El Niño. Part I: Mechanisms of oceanic change. *Journal of Climate*, *19*(12), 2633–2646. https://doi.org/10.1175/JCLI3776.1

Vialard, J., Menkes, C., Boulanger, J.-P., Delecluse, P., Guilyardi, E., McPhaden, M. J., & Madec, G. (2001). A model study of oceanic mechanisms affecting equatorial Pacific sea surface temperature during the 1997–98 El Niño. *Journal of Physical Oceanography*, *31*(7), 1649–1675. https://doi.org/10.1175/1520-0485(2001)031%3C1649:AMSOOM%3E2.0.CO;2

Wang, B., Wu, R., & Lukas, R. (1999). Roles of the western North Pacific wind variation in thermocline adjustment and ENSO phase transition. *Journal of the Meteorological Society of Japan. Ser. II*, *77*(1), 1–16. https://doi.org/10.2151/jmsj1965.77.1_1

Webster, P. J. (1973). Remote forcing of the time-independent tropical atmosphere. *Monthly Weather Review*, *101*(1), 58–68. https://doi.org/10.1175/1520-0493(1973)101%3C0058:RFOTTT%3E2.3.CO;2

Wittenberg, A. T., Rosati, A., Delworth, T. L., Vecchi, G. A., & Zeng, F. (2014). ENSO modulation: Is it decadally predictable? *Journal of Climate*, *27*(7), 2667–2681. https://doi.org/10.1175/JCLI-D-13-00577.1

Wyrtki, K. (1985). Water displacements in the Pacific and the genesis of El Niño cycles. *Journal of Geophysical Research: Oceans*, *90*(C4), 7129–7132. https://doi.org/10.1029/JC090iC04p07129

Xie, R., & Jin, F.-F. (2018). Two leading ENSO modes and El Niño types in the Zebiak-Cane model. *Journal of Climate*, *31*(5), 1943–1962. https://doi.org/10.1175/jcli-d-17-0469.1

Yu, L., Weller, R. A., & Liu, T. W. (2003). Case analysis of a role of ENSO in regulating the generation of westerly wind bursts in the western equatorial Pacific. *Journal of Geophysical Research*, *108*(C4), 3128. https://doi.org/10.1029/2002JC001498

Zavala-Garay, J., Zhang, C., Moore, A. M., & Kleeman, R. (2005). The linear response of ENSO to the Madden-Julian Oscillation. *Journal of Climate*, *18*, 2441–2459. https://doi.org/10.1175/JCLI3408.1

Zebiak, S. E. (1982). A simple atmospheric model of relevance to El Niño. *Journal of the Atmospheric Sciences*, *39*(9), 2017–2027. https://doi.org/10.1175/1520-0469(1982)039<2017:Asamor>2.0.Co;2

Zebiak, S. E., & Cane, M. A. (1987). A model El Niño-Southern Oscillation. *Monthly Weather Review*, *115*(10), 2262–2278. https://doi.org/10.1175/1520-0493(1987)115<2262:Ameno>2.0.Co;2